Energy LAB

REVIEW ARTICLE

Energy Lab 2023, 1, 230004

Strain management in perovskite solar cells

Yuanyuan Zhao[1*], Qiurui Wang[1], Yinping Teng[1], Zhe Xin[1], Yusheng Cao[1], Jialong Duan[2], Qiyao Guo[2], Yingli Wang[2] and Qunwei Tang[2*]

Perovskite solar cells (PSCs) currently hold the record for highest power conversion efficiency (PCE) at an impressive 26.1%. However, the state-of-the-art PCEs still fall below theoretical limits, and the long-term stability remains a critical concern for practical implementation of PSCs. Due to the soft ionic nature of metal halide perovskites, the inevitable strain effect on perovskite films has been found to be a key factor in determining both efficiency and stability. In this review, we summarize the recent advancements on the origins of strain, the characterization methodologies, and the impact of strain on perovskite films, as well as various strategies employed to regulate strain and enhance the intrinsic performance of perovskites and solar cells. Our intention is to facilitate scientists with an exhaustive comprehension of the strain effect, and stimulate research endeavors in strain management aimed at enhancing device performance and commercialization.

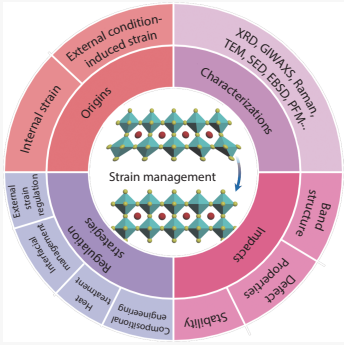

The escalating global energy crisis and environmental pollution, driven by an insatiable human demand for energy and excessive utilization of fossil fuels, represent significant challenges that require immediate attention. In this context, the exploration of sustainable and clean energy sources, such as solar energy and hydrogen, has gained considerable traction.[1–2] Among them, solar energy is the most abundant, renewable, and environmentally benign option, capable of meeting a significant proportion of the world's energy needs. In this regard, perovskite solar cells (PSCs) have emerged as a highly promising technology with exceptional potential for revolutionizing the solar energy landscape. Over the past decade, PSCs have attracted considerable attentions due to their tunable bandgap,[3] efficient optical absorption,[4] cost-effective solution processing, high charge carrier mobility,[5] and low recombination rate.[6] Through systematic study of perovskite film preparation processes, interface engineering, component engineering, spectral engineering, and strain regulation, the power conversion efficiency (PCE) of single junction devices has rapidly improved from 3.8% to a certified 26.1%.[7] Nonetheless, the commercialization of these promising PSCs is still impeded by serious challenges, including instability against external stimuli such as moisture, heat and light. To overcome this, it is imperative to focus more intently on understanding the origins of the intrinsic instability and enhancing the stability of PSCs. Among these, the soft ionic nature of halide perovskites makes them susceptible to strain, which has recently been recognized as a pivotal factors that influences their photovoltaic performance and device stability.

Residual strain in perovskites can arise from a variety of sources, including $[BX_6]^{4-}$ octahedral tilts,[8] heterogeneous crystallization,[9] lattice and thermal expansion mismatch,[10] and external stress conditions.[11] However, tensile strain in perovskites weakens chemical bonds, reduces the activation energy of ion migration and the formation energy of additional defects, and increases non-radiative recombination, which significantly promotes chemical composition degradation and fracture of perovskite films induced by light, heat and moisture.[12–14] Tensile strain-induced intrinsic instability is now widely recognized as a major bottleneck toward achieving high-efficiency and stable PSCs. Conversely, some studies show that slight compressive strain is beneficial for the photovoltaic performance and stability of PSC.[9,15–16] For instance, applying appropriate hydrostatic pressure can narrow the bandgap of $MAPbI_3$/$FAPbI_3$, broadening the absorption spectrum and optimizing energy level alignment, while prolonging carrier lifetime, resulting in enhanced photovoltaic performance.[13,17–18] To maximize the optoelectronic properties of halide perovskites and achieve high PCE and stability in PSCs, a thorough understanding of the origins, classical characterization techniques, implications, and strain-regulation strategies is essential.

At present, our understanding of how to manipulate strains in halide perovskite films is lacking in-depth, and an overview of this topic is urgently needed. In this review, we summarize

[1] *College of Mechanical and Electronic Engineering, Shandong University of Science and Technology, Qingdao 266590, China*

[2] *Institute of Carbon Neutrality, College of Chemical and Biological Engineering, Shandong University of Science and Technology, Qingdao 266590, China*

* Corresponding author, E-mail: yuanyuanzhao@sdust.edu.cn; tangqunwei@jnu.edu.cn

Received 2 February 2023; Accepted 10 May 2023; Published online

DOI: 10.54227/elab.20230004

the recent progress made in understanding the origins of strain, state-of-the-art characterization techniques, and the impacts of strain on both perovskite films and solar cells, as well as the various strain-regulation strategies for improving the intrinsic photovoltaic performance. We begin by discussing the two different origins of stain in halide perovskites: (i) internal strain originating from $[BX_6]^{4-}$ octahedral tilts[8] and heterogeneous crystallization,[9] and (ii) external condition-induced strain, including lattice and thermal expansion mismatch,[10] and external stress conditions.[11] We then review the state-of-the-art characterization methods for strain, including X-ray diffraction (XRD), grazing incidence X-ray diffraction (GIXRD), grazing-incidence wide-angle X-ray scattering (GIWAXS), Raman spectroscopy, transmission electron microscopy (TEM), scanning electron diffraction (SED), electron back-scattered diffraction (EBSD), and piezoresponse force microscopy (PFM).[11] Subsequently, we summarize the impacts of strain on perovskite film and device performance, including its effects on band structure, defect properties and stability (ion migration, phase and device stability). Finally, we summarize recent advances in strain-regulation methods, such as compositional engineering, heat treatment strategies, interfacial management, and external strain regulation. We try to provide a perspective on further strain-regulation innovations and enhance research activity in strain management to further improve device performance toward commercialization.

Strain in perovskite films

Strain (ε) refers to the relative deformation of a crystal structure due to external stress and other factors. It can be described as:

$$\varepsilon = \frac{(a_0 - a)}{a_0} \quad (1)$$

where a_0 and a are the lattice constants for unstrained and strained materials, respectively.[14] Tensile strain occurs when the lattice length increases under stress, while compressive strain arises from lattice compression or decrease under stress.[19] In perovskites, strain can originate from either internal or external factors.

Internal strain in perovskite films

Internal strain, a type of strain that arises intrinsically within halide perovskite crystals, is not induced by external stress, but rather emerges from non-periodicity within the crystal lattice. This strain primarily arises from $[BX_6]^{4-}$ octahedral tilts and heterogeneous crystallization.

Metal halide perovskites, represented by the general formula ABX_3,[20] consist of a monovalent cation, such as methylammonium ($CH_3NH_3^+$, MA^+), formamidinium ($CH(NH_2)_2^+$, FA^+), cesium (Cs^+) or substituted by alkali metal ions. B-site cations include divalent lead (Pb^{2+}), tin (Sn^{2+}), and germanium (Ge^{2+}) ions (Figure 1a), which can be doped by divalent alkaline earth metal ions, transition metal ions, or trivalent rare earth metal ions.[21] X-site anions generally consist of halide ions including chlorine (Cl^-), bromine (Br^-), and iodine (I^-) species.[22] The Goldschmidt tolerance factor $(t = \frac{R_A + R_X}{\sqrt{2}(R_B + R_X)})$ provides an empirical rule for assessing perovskite structure stability, where R_A, R_B and R_X representing the corresponding ions radii. Metal halide perovskites tend to exhibit an ideal cubic structure at $0.8 < t < 1$, an orthorhombic structure at $t < 0.8$, and a hexagonal structure at $t > 1$.[23–24] The cubic phase is considered the most desirable structure for metal halide perovskites. However, when the A-cation's radius is too large or too small compared to the rest of B-X cage, it causes cage dis-

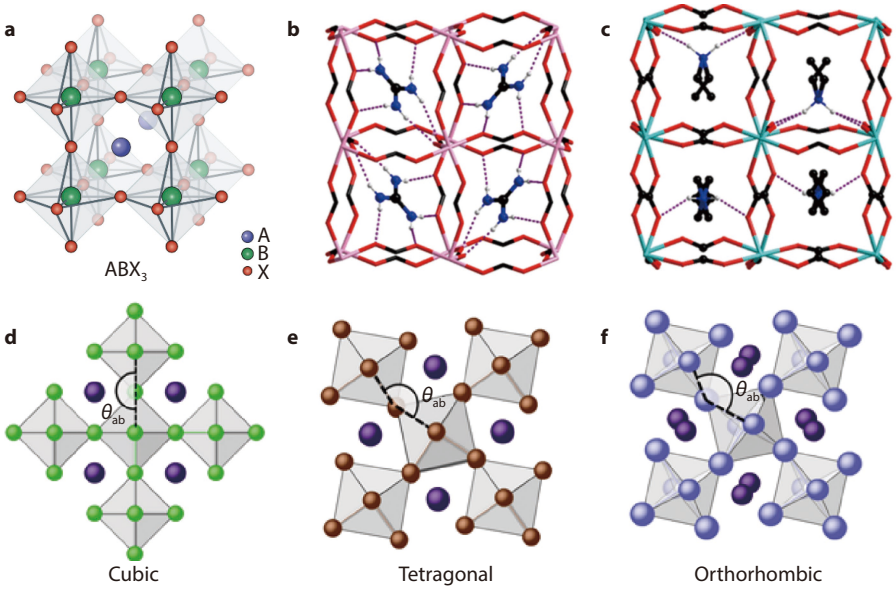

Fig. 1 **a** A general perovskite structure with the stoichiometric formula of ABX_3.[21] Copyright 2014, The Journal of Physical Chemistry C. Structural diagram of **b** (GUA)[$Mn(HCOO)_3$] (GUA-1) and **c** (AZE)[$Mn(HCOO)_3$] (AZE-2) viewed along the (10"1) direction. Only H atoms bonded with N atoms are shown for demonstration, and the N-H·O hydrogen bonds are represented as dashed lines. Color scheme: Mn, rose or aqua; N, blue; C, black; H, light gray.[30] Copyright 2019, Coordination Chemistry Reviews. Typical crystal phases of ABX_3 MHPs including **d** cubic phase, **e** tetragonal phase and **f**, orthorhombic phase. The symmetry descent is related to small coherent displacements of halides, leading to bending of Pb- X-Pb angles with $\theta_{ab} = \theta_c = 180°$, $\theta_{ab} < 180°$ and $\theta_c = 180°$, and $\theta_{ab} = \theta_c < 180°$.[34] Copyright 2017, ACS Nano.

DOI: 10.54227/elab.20230004

tortions and octahedra tilting,[25] leading to atomic displacements and/or ionic mismatch that generate local lattice strain. For example, the difference sizes of A cations lead to tensile strain in the (111) plane[26] of $FAPbI_3$ ($t > 1$)[27] and compressive strain in $MAPbI_3$ ($t < 1$)[27] and $CsPbI_3$ ($t < 1$).[28] Sargent *et al*.[8] observed that mixed CsMAFA perovskites exhibit better stability than $FAPbI_3$, with the later being susceptible to local lattice strain resulting from the large size of FA^+ cation. This classical ion size mismatch between the FA^+ cation and the Pb iodide cage causes cage distortion and PbI_6 octahedral tilting.

Although steric effects dominate the octahedral tilt in inorganic halide perovskites such as $CsPbX_3$, the hydrogen bonding between the organic A-site cations and the halide frame also plays a role in determining octahedral tilts in hybrid perovskites, for example, $MAPbI_3$ and $FAPbI_3$.[29] Li *et al*.[30] reported a significant difference (up to a factor of two) in the mechanical properties of two organic-inorganic hybrid perovskites, (GUA) $[Mn(HCOO)_3]$ (GUA-1, GUA = guanidinium) (Figure 1b) and (AZE) $[Mn(HCOO)_3]$ (AZE-2, AZE = azetidinium) (Figure 1c), which can be arributed to their distinct modes of hydrogen bonding between the A-site amine cations and the $[Mn(HCOO)_3]^-$ framework host. Such lattice expansion or contraction is often accompanied by a phase transition. For example, $CsPbI_3$ has four different crystalline phases (the cubic phase [α], tetragonal phase [β], orthogonal phase [γ], and the yellow hexagonal phase [δ]).[19] The ideal cubic α-$CsPbI_3$ perovskite consists of corner sharing $[PbI_6]^{4-}$ octahedra with Cs^+ cations 12-fold coordinated, occupying the cubic centers formed by eight octahedra.[31] In non-perovskite δ-$CsPbI_3$, the octahedra are edge-sharing and double chains are connected by 9-fold coordinated Cs^+ cations, resulting in tilted octahedra.[32–33] Generally, the cubic α-$CsPbI_3$ phase exhibits a more symmetric structure, while the δ phase is more complex and less symmetric.

It should be noted that lattice distortion can also arise from the changes in the length and angle of B-X-B bonds. For example, metal halide perovskites often undergo a phase transition from the cubic phase to tetragonal or orthogonal phase as the B-X-B bond angle decreases (Figure 1d-f).[34] In $CsPbX_3$ perovskites, the Pb atoms occupy the nodes of a (pseudo) cubic lattice and are octahedrally coordinated by halides, while the Cs ions rattle near the center of the cube. Due to the high flexibility of the PbX_6 octahedra-based framework in three dimensions (3D) and the halide size, $CsPbX_3$ perovskites may exhibit archetypal cubic structure or lower symmetries, mainly resulting from the tilting of the octahedra-based octahedra implying bending of the Pb-X-Pb angles from the ideal 180° value, indicating the cubic, tetragonal, and orthorhombic structures as the α, β, and γ-phases, respectively. At standard bulk conditions, the thermodynamically stable polymorphs are perovskite structures (3D connectivity of corner-sharing PbX_6 octahedra), with cubic (though debatable) for X = Cl and orthorhombic for X = Br, and for X = I, a nonperovskite orthorhombic polymorph (δ-phase, 1D connectivity of edge-sharing PbX_6 octahedra, with a wider energy bandgap, PL inactive).

Local lattice mismatch is another critical source of internal strain in perovskites, particularly in the case of mixed halide perovskites,[9] which exhibit material inhomogeneity due to the separation of Br-rich and I-rich phases under the attacks of heat and light. The lattice strain arises during film crystallization and induces the formation of defects due to significant chemical mismatch among individual components and nonequilibrium growth conditions. Multiscale analyses involving correlated synchrotron scanning XRD and time-resolved photoluminescence (TRPL) measurements on the same scan area have revealed that lattice strain is directly proportional to enhanced defect concentration and nonradiative recombination,[10] subsequently influencing the optoelectronic properties of perovskite films. In-plane residual strain gradient distribution in perovskite films has been detected by Chen *et al*., closely associated with lattice structure evolution due to compositional inhomogeneity perpendicular to the substrate.[35] Mela *et al*. [36] have reported a significant change in Young's modulus (YM) in perovskite films, with a sudden increase in YM at grain boundaries, sometimes by more than an order of magnitude. Spatially averaged values of YM were determined to be 9.1 ± 2.6 GPa, revealing marked variations in the bulk (6.9 ± 1.3 GPa) and boundary regions (12.5 ± 2.9 GPa) of $Cs_{0.05}MA_{0.17}FA_{0.78}Pb(I_{0.83}Br_{0.17})_3$ mixed-halide perovskite films. The elevated YM is attributed to the accumulation of bromides residing preferentially at the boundaries of morphological grains, but also occur in specific intragrain regions, leading to composition heterogeneity. YM may also vary within the same morphological grains, revealing the presence of subcrystalline zones and even greater structural inhomogeneity.

Additionally, local crystal misorientation generates local strain at perovskite grains, and the grain-to-grain orientation spread further induces local strain heterogeneity in perovskite films (Figure 2a). Grain boundaries with specific interfacial conditions constitute another source of strain (Figure 2b), with striking variation in orientation mismatch at these boundaries.[37–38] Jariwala *et al*.[38] employed plots of grain orientation spread (GOS) to demonstrate the presence of grain-to-grain heterogeneity in the average local misorientation of $CH_3NH_3PbI_3$ perovskite film (Figure 2d). They observed a wide range of GOS values, ranging from 0 (perfectly ordered) to 4.3, indicative of significant variations in orientation spread within individual grains. These variations in crystal orientation suggest the existence of local strain distributions within the grains. Higher GOS values correspond to grains with higher strain, whereas lower GOS values correspond to grains with lower strain. Furthermore, subgrain lattice orientation disorder (Figure 2c) may contribute to strain in halide perovskite films.[37] Jariwala *et al*. [37] have demonstrated that such strain depends heavily on the orientation of grains and interfaces between them using EBSD.

External condition-induced strain

In general, the thermal stress can be expressed as:

$$\sigma_{\Delta T} = \frac{E_p}{1 - V_p}\left(\alpha_s - \alpha_p\right)\Delta T \quad (2)$$

During the annealing process after the precursor liquid has been coated onto the solid substrate, there is a thermal expansion mismatch between the perovskite film and substrate that causes strain in the perovskite layer.[19] Figure 2e provides a comparison of the linear thermal expansion coefficients (α) of commonly used lead halide perovskites, sub-

DOI: 10.54227/elab.20230004

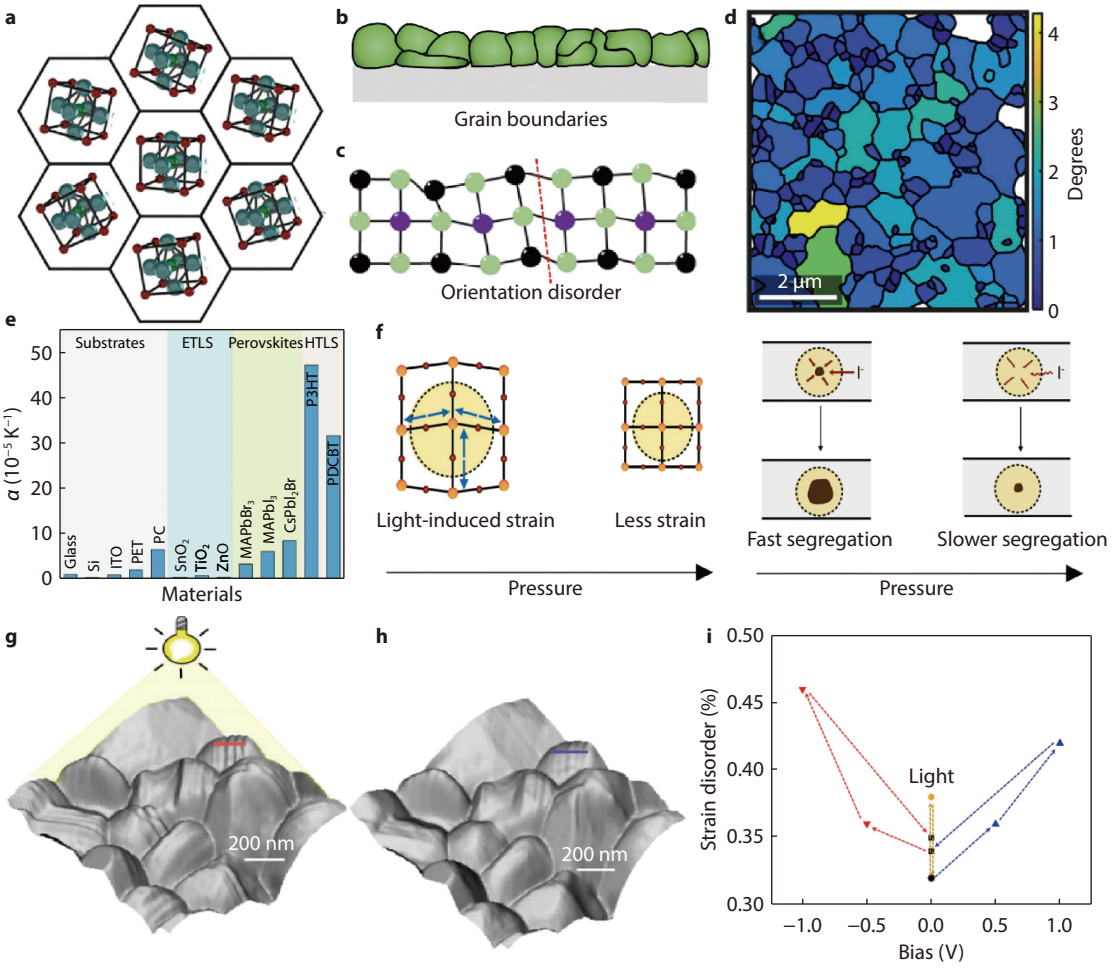

Fig. 2 **a** Schematic illustration of sub-grain orientation heterogeneity induced stain in $CH_3NH_3PbI_3$ perovskite films.[37] Copyright 2019, Joule. **b** Grain boundaries. **c** The purple spheres are the A-site cations, and the black and green spheres represent metal cations and halide anions, respectively. The red dashed line in *c* indicates a twin boundary.[38] Copyright 2021, Nature Materials. **d** Plot of grain orientation spread (GOS) showing grain-to-grain heterogeneity in average local misorientation in the same film.[37] Copyright 2019, Joule. **e** Thermal expansion coefficients of functional layers in PSCs including perovskites, substrates, ETLs and HTLs.[15] Copyright 2020, Nature Communications. **f** Illustrations of strain pressure and light-induced strain, which affects the rate of halide segregation in mixed-halide perovskites.[40] Copyright 2020, ACS Energy Letters. Morphological imaging of $(FAPbI_3)_{0.85}(MAPbBr_3)_{0.15}$ perovskite film surface **g** under light, showing distinct corrugated surfaces, and **h** without light, where the surface is smoother. **i** The effect of applied electrical bias and illumination on strain disorder in such perovskite.[42] Copyright 2019, Nature Communications.

strates, and other functional layers, such as electron-transport layers (ETLs) and hole-transport layers (HTLs). The lattice mismatch between the perovskites and substrates, as well as their interactions, restricts the free expansion or contraction of the thin perovskite film.[19] Since the perovskite has a higher α value, the corresponding cubic perovskite volume thermal expansion coefficient (α_v) is larger than that of Cu (In, Ga) Se_2 and CdTe. The ITO-coated glass and metal oxide charge transport layers that are widely used have much lower α values in the range of 0.37 to 1×10^{-5} K^{-1}. Thus, there is a significant thermal expansion difference between the perovskite film and substrate.[10] As a result, the perovskite layer has a large shrinkage rate, causing tensile strain in the perovskite layer.[39] In general, the thermal stress($\sigma_{\Delta T}$) can be expressed as:

where E_p represents the Young's modulus of the perovskite, v_p represents the Poisson's ratio of the perovskite, α_p and α_s are the thermal expansion coefficients of perovskite and substrate, respectively, and ΔT is the temperature difference between annealing and operating processes. Hence, the residual strain/stress is determined by various factors.

The lattice mismatch between the perovskite and epitaxial substrate is another source of strain, and it has been a long-standing challenge to select an epitaxial substrate with an suitable mismatched lattice for chemical epitaxy. The strain introduced by lattice mismatch is critical to the structure parameters of the resulting thin film. As the film thickness increases, the strain will be eventually released through a series of misfit dislocations perpendicular to the substrate film interface.[19]

External stimuli, such as illumination, temperature, electrical bias, and external pressure can also induce additional strain in perovskite during the operation of PSCs.[11] Under illumination, the expansion of the lattice can trigger structural distortion, resulting in tensile strain. Chen *et al*. demonstrated that the thermal expansion in $MAPbI_3$ perovskites upon illumina-

DOI: 10.54227/elab.20230004

tion was mainly responsible for photo-induced strain.[35] This thermal expansion often leads to a reduced activation energy for halide vacancies, inducing ion migration, weakened Pb-X bond, and hence tensile strain (Figure 2f).[40] Tsai *et al*. also reported that the continuous illumination led to uniform lattice expansion in a hybrid perovskite film, which could release local lattice strain and reduce the interface energy barrier.[41] Mela *et al*. found that light-activated ion migration drove phase homogenization in the perovskite film and caused a uniform distribution of mechanical properties.[36]

Under illumination, the polarity (positive or negative) and magnitude of the bias voltage have also been shown to induce strain by enhancing ion migration. Kim et al. studied the impacts of illumination and electric bias on the strain of perovskite surface.[42] Besides the strain disorder induced by illumination, a positive electrical bias induces a corrugated surface morphology (Figure 2g–i), while a negative bias causes the removal of these uneven features. Strelcov *et al*. have also demonstrated an increase/decrease in piezoresponse under applied negative/positive bias, which may be due to the change of local ion concentration under the electric field, since ion migration affects the local strain.[43] Moreover, Liu *et al*. showed that $MAPbI_3$, $CsPbIBr_2$ and PEA_2PbI_4 perovskites exhibited lattice expansion upon the stimuli of both external light and heat, whereas the lattice of $FAPbI_3$ only expanded upon additional temperature. By applying hydrostatic pressure to the perovskite film or bending its substrate (in the case of a flexible foil), the bond lengths and angles of the perovskite lattice can be modified to induce compressive or tensile strains.[13] In addition, the mechanically soft nature of perovskites means that they are particularly prone to strain, so strain is a concern because it can cause several adverse processes, such as perovskite degradation.

Characterization methods for strain in perovskite film

XRD

XRD is a fundamental characterization technique for assessing strain in halide perovskites, given that strain directly modifies the lattice parameters. Through the application of Bragg's law ($2d\sin\theta = n\lambda$), the strain can be determined by measuring the shift of XRD peaks. Specially, tensile strain leads to an increase in the *d*-spacing, whereas compressive strain causes a decrease in the *d*-spacing. As a consequence, XRD peaks shift towards lower angles when subjected to tensile strain and towards higher angles when subjected to compressive strain.

Standard XRD characterization techniques are typically limited to relatively large sample area and thus cannot resolve strain on a micro- or nano-scale. Additionally, strain in most materials is non-uniform and complex, making it difficult to simply differentiate as either tensile or compressive. In this case, an indicator of strain is the broadening of XRD peaks compared with that of the strain-free material.[45] To quantify the amount of strain, the Williamson-Hall equation is commonly employed:

$$\beta_{hkl}cos\theta = 4\epsilon sin\theta + \frac{K\lambda}{D} \quad (3)$$

where β_{hkl} is the width of the XRD peak at full width at half maximum (FWHM), ε is the strain, k is the Scherrer constant, λ is wavelength of the X-ray radiation, and D is crystallite size. By plotting $\beta_{hkl}\cos\theta$ as a function of $4\sin\theta$, the slope of the resulting line can be used to determine the strain ε. A negative slope indicates that the strain is tensile in nature, while a positive slope indicates compressive strain.

XRD measurements can be divided into in-plane and out-of-plane measurements. The former characterizes the spacing of crystal planes parallel to the substrate, while the latter characterizes the spacing of crystal planes perpendicular to the substrate, as illustrated in Figure 3a.[13] However, a limitation of standard reflection-mode XRD is that it can only detect out-of-plane strain, whereas in-plane strain can arise due to the Poisson's effect. GIXRD measurements can detect both out-of-plane and in-plane strain (Figure 3b). This technique can also be used to study the depth-dependent strain distribution in perovskite films. Depth-gradient information can be obtained by changing the incident angel, whereby a larger incident angle results in deeper X-ray penetration from the surface (Figure 3c-e). Chen *et al*.[35] conducted GIXRD measurements to study the evolution of in-plane residual strain as a function of film thickness in mixed perovskite films. Their findings revealed similar XRD patterns in the depth range of 50~500 nm, suggesting the same cubic phase structure at different depths. However, the diffraction peaks systematically shifted to lower angles with increasing penetration depth, indicating the inhomogeneity of tensile strain in the perovskite film (Figure 3c). This method can also be used to characterize compressive strain and no-strain in perovskite films (Figure 3d-e). By combining classical $\sin^2\varphi$ measurements with GIXRD (Figure 3b, f), the slope of the fitting line in the linear relationship between $\sin^2\varphi$ and 2θ can be used to determine the magnitude of strain (Figure 3g). These results demonstrate the gradient distribution of tensile strain in perovskite films, with the tensile strain decreasing gradually from the surface to the bulk. This method can also be used to monitor compressive strain, as shown in (Figure 3h). In a perovskite film, if there is tensile strain in one direction, there is compressive strain in the other direction, and the shift of the in-plane XRD peak is opposite to that of the out-of-plane XRD peak. If the peak shift is only caused by composition rather than strain, the in-plane and out-of-plane XRD results will be the same.

GIWAXS

GIWAXS has been shown to be a valuable tool in the study of perovskite materials.[46] GIWAXS data are typically two-dimensional diffractograms that display diffraction rings corresponding to different crystal planes. GIWAXS measurements provide information on the crystal orientation and crystallization quality of perovskite films, as well as the stacking manner of grains at various depths, which is crucial for understanding the crystallization mechanism. In-situ measurements allow for the rapid tracking of microstructural changes in perovskite materials, including the crystallization and aging processes, which are essential for understanding the kinetics of perovskite materials.[46] The lattice strain causes asymmetric growth of the crystal, resulting in structural instability and thus the formation of δ-phase.

In order to determine the corresponding perovskite phase,

DOI: 10.54227/elab.20230004

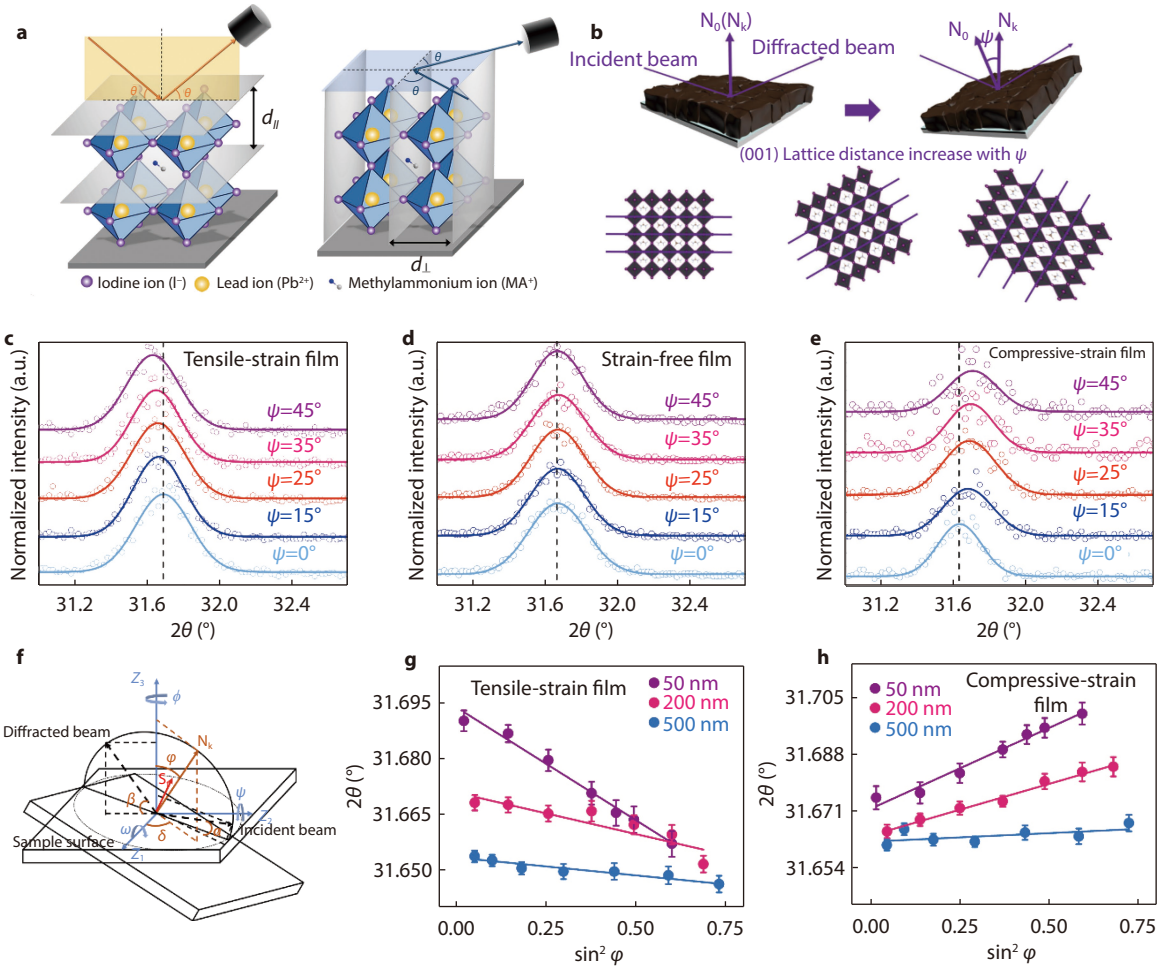

Fig. 3 **a** The differentiation between out-of- and in-plane diffraction-based characterizations.[13] Copyright 2017, Science Advances. **b** Illustration of how tilting the instrument angle c allows to obtain difference between the sample normal vector (N_0) and scattering vector (N_k). XRD reflections of the same sample at different grazing angles under **c** tensile strain, **d** no strain and **e** compressive strain. **f** Diffraction geometries of depth-dependent strain distribution measurement. Strain distribution at depths of 50, 200 and 500 nm as a function of $\sin^2\varphi$ for the **g** tensile-strained and **h** compressive-strained film. The error bar represents the standard deviation of 2θ.[35] Copyright 2019, Nature Communications.

lattice parameters of perovskite were measured using GIWAXS measurements. Clear information regarding the lattice parameters of perovskite by analyzing the GIWAXS images was shown in Figure 4a.[47] Hui *et.al.*[48] used in situ GIWAXS to systematically investigate the crystal growth dynamics at different processing temperatures. The crystallization evaluation of perovskite films at varying processing temperatures and annealing times (Figure 4b, c) revealed that increasing the processing temperature up to 55 °C resulted in excellent perovskite phase crystallinity with the strongest peak at q=10 nm^{-1} and phase stability with no δ phase observed. Additionally, the crystal lattice shown the minimum strain.

Recently, Wu *et al.*[49] utilized MXene to passivate the surface of SnO_2 ETL film. The GIWAXS pattern of SnO_2-MXene/perovskite displayed a brighter scattering ring at q≈10.0 nm^{-1} (Figure 4d, e), indicating that SnO_2-MXene/perovskite exhibits better crystallinity and out-of-plane orientation due to MXene materials' matching lattice with CsFAMA perovskite. They speculated that the lattice matching of MXene and perovskite suppresses stress concentration caused by the interface mismatch during the perovskite annealing and cooling processes, resulting in high-quality oriented perovskite films. Chen *et al.*[50] further analyzed the surficial structural properties of the perovskite films by GIWAXS (Figure 4f, g), with an angle of incidence set to 0.3°. Both the control and target perovskite films exhibited identical Bragg reflections and orientation for the perovskite phase, indicating that BMI modification had little impact on the crystallization of perovskite film, and no new phases are formed.

Raman spectroscopy

Raman spectroscopy is another technique that can be employed for the detection of strain. Xu *et al.*[16] utilized this method to investigate the structural properties of α-$FAPbI_3$ under strains ranging from 0% to -2.4%. The peak at 136 cm^{-1} exhibited a split into two distinct peaks at 140 cm^{-1} (main) and 133 cm^{-1} (shoulder) (Figure 5a-b). These peaks shifted to 143 cm^{-1} and 130 cm^{-1} as the strain was further increased to −2.4%. The compression in-plane Pb-I bond was assigned to the blue shift of the main peak, whereas the red shift of the shoulder peak was attributed to the stretching of out-of-plane Pb-I bond.

Badrooj *et al.*[51] compared the Raman spectra obtained

DOI: 10.54227/elab.20230004

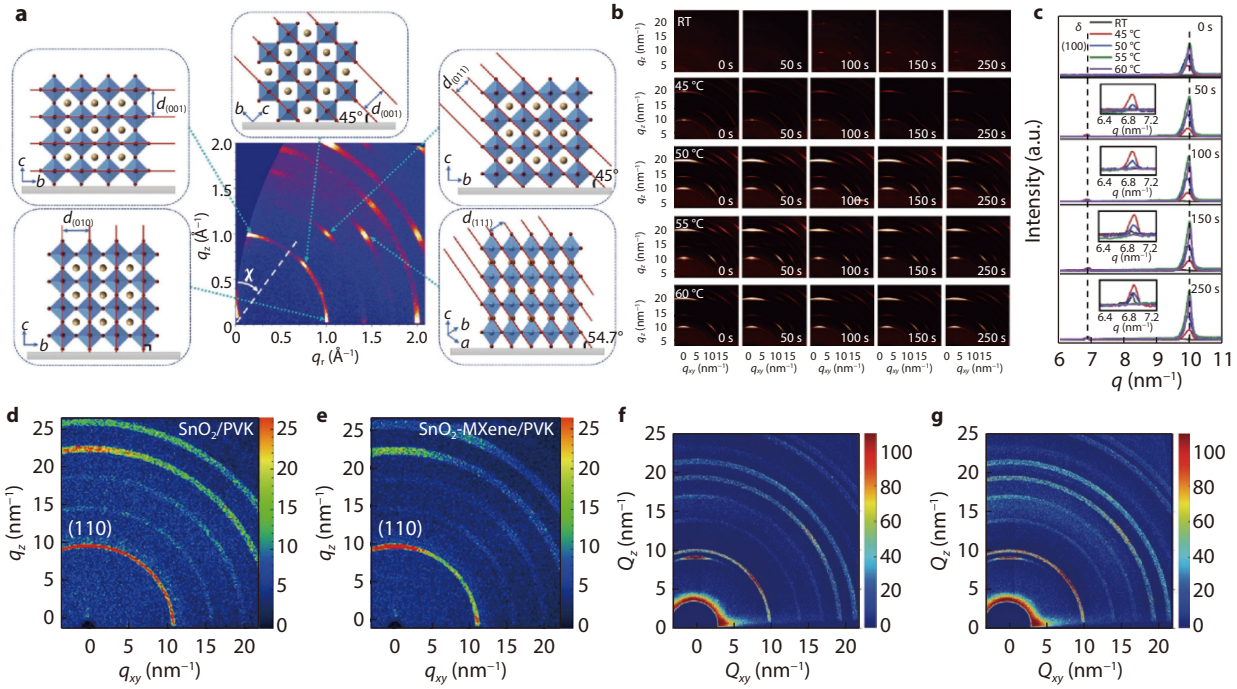

Fig. 4 **a** A schematic illustration of the GIWAXS pattern obtained from a highly oriented 3D perovskite film.[47] Copyright 2021, Advanced Materials. **b** Time-varying map of 2D- GIWAXS spectra of perovskite films at different processing temperatures under different annealing time. **c** Comparison of one dimensional GIWAXS integral at RT-casting (black), 45 °C-casting (red), 50 °C -casting (blue), 55 °C -casting (green), and 60 °C -casting (purple) under different annealing time.[48] Copyright 2020, Nano Energy. GIWAXS patterns of **d** SnO_2/PVK and **e** SnO_2-MXene/PVK film. SnO_2-MXene induces oriented growth of PVK.[49] Copyright 2022, Angewandte Chemie International Edition. GIWAXS 2D reciprocal space maps of **f** control sample and **g** target sample.[50] Copyright 2022, Advanced Functional Materials.

from pure $MAPbI_3$, $MASnI_3$, and FTO/porous-TiO_2 substrates at room temperature (Figure 5c). Table 1 summarizes the active Raman modes observed in the $MAPbI_3$ and $MASnI_3$ spectra. In the Raman spectroscopy, By utilizing the variation of vibration frequency versus residual strain values as a calibration curve, the amount of compressive strain of $MASn_xPb_{1-x}I_3$ layers can be estimated using equation 4 based on the information acquired from the shift of vibrational modes in the experimental Raman spectra.

$$\frac{\Delta\omega^{\pm}}{\Delta\omega_0} = -\gamma(1-\upsilon)\varepsilon_z \quad (4)$$

where ω_0 and $\frac{\Delta\omega^{\pm}}{\Delta\omega_0}$ represent the peak position under zero strain and the relative shift of the Raman band, respectively. The Gruneisen parameter (γ) is estimated to be 1.6 for polycrystalline perovskite. υ and ε_z represents Poisson's ratio (about 0.3 on average) and compressive strain, respectively. As the vibration frequency in the material shifts with the strain, this phenomenon can be utilized to map the local strain in the perovskite material using Raman spectroscopy. For instance, a reversible structural transition from orthorhombic to monoclinic phase at 3.9 GPa for $CsPbI_3$ was successfully characterized using Raman spectroscopy at room temperature.[52] The Raman mapping images were characterized by Zhou *et al.*,[53] as illustrated in Figure 5d, e. The pristine $CsPbBr_3$ perovskite film exhibits a serious tensile strain, resulting in a lower average wavenumber around 295 cm^{-1} for Cs^+ vibrational mode in Figure 5f. This is mainly formed during the annealing process owing to the different thermal expansion coefficients of adjacent layers in the PSC devices. Higher tensile strain results in more severe lattice distortion, larger charge transfer barriers, and lower ions migration energy. However, the introduction of $Ti_3C_2Cl_x$ MXene into the $CsPbBr_3$ film results in a homogeneously distributed Raman peak for Cs^+ vibrational mode that is closer to 309 cm^{-1} (Figure 5e-f), clearly indicating the released tensile strain in the perovskite film.

TEM

Strain contrast is a primary contrast mechanisms for microstructure imaging in TEM of crystalline materials. This imaging technique measures local lattice parameter changes and lattice plane orientations relative to a reference material. To date, four primary TEM techniques have been developed to measure strain, including convergent-beam electron diffraction (CBED),[54] nano-beam electron diffraction (NBED),[55–56] high-resolution TEM (HRTEM), and dark-field electron holography (DFEH).[57]

Currently, the CBED technique is the only method capable of providing quantitative strain information with nanometer-scale resolution in TEM. This point-to-point method obtains the strain tensor at each nanoregion of the sample probed by the electron beam by analyzing the corresponding diffraction pattern. The CBED method is based on the shift of high-order Laue zone (HOLZ) deficiency lines induced by strain in the central disk of a convergent beam pattern, taken in a zone axis where the HOLZ lines are free from dynamical interactions. Strain and lattice are measured from the shift of the line positions. However, sufficient HOLZ scattering requires the crystal to be oriented in a relatively high-order zone axis. The

DOI: 10.54227/elab.20230004

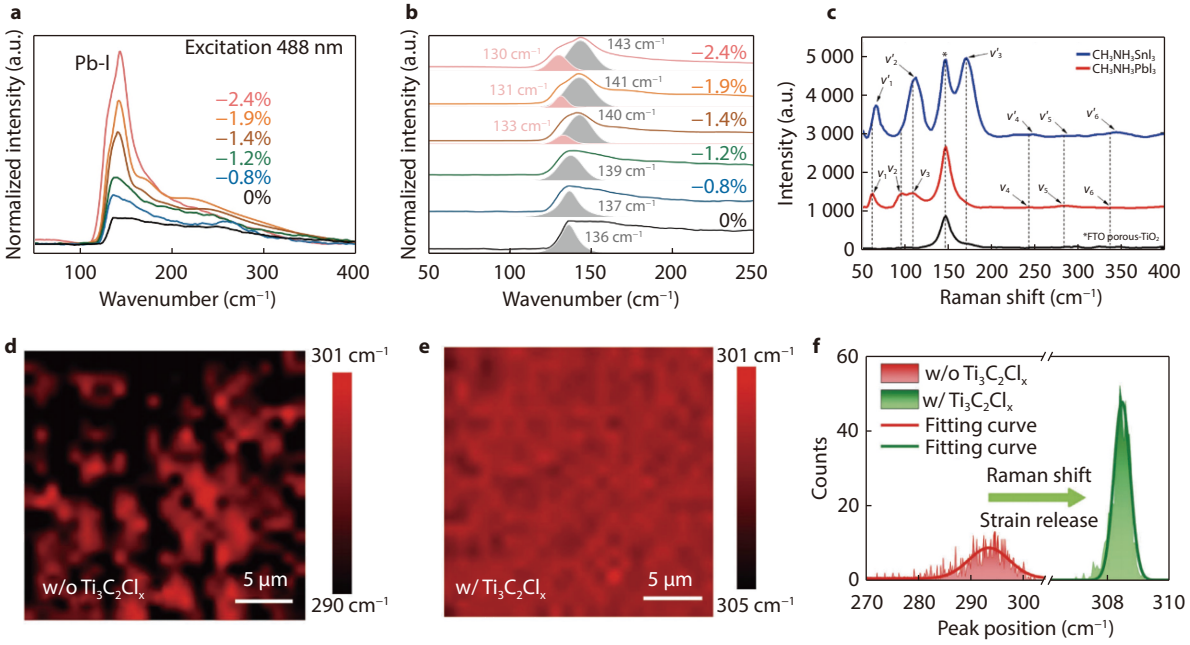

Fig. 5 **a** Confocal Raman spectra of the epitaxial α-$FAPbI_3$ layer at different strains. **b** Fitting analysis of the Raman peaks in **a**.[16] Copyright 2020, Nature. **c** Raman spectra obtained from pure $MAPbI_3$, $MASnI_3$, and FTO/porous-TiO_2 substrate.[51] Copyright 2020, The Journal of Physical Chemistry C. Raman mapping images of $CsPbBr_3$ perovskite films **d** without and **e** with $Ti_3C_2Cl_x$ MXene, and **f** the corresponding distribution statistics of Raman peak for different perovskite films.[53] Copyright 2021, Advanced Science.

Table 1. Active Raman Bands of $CH_3NH_3PbI_3$ and $CH_3NH_3SnI_3$ in the Tetragonal-RT Phase.[51] Copyright 2020, The Journal of Physical Chemistry C.

Samples	Raman bands	Wavenumber (cm^{-1})	Assignments
$MAPbI_3$	v_1	62.54	I-Pb-I bending mode
	v_2	95.71	libration modes of the organic cations coupled to Pb-I stretching
	v_3	108.58	MA librational mode
	v_4	243.50	MA torsional mode
	v_5	283.22	MA torsional mode
	v_6	342.47	MA torsional mode
$MASnI_3$	v'_1	66.23	I-Sn-I bending mode
	v'_2	112.26	libration modes of the organic cations coupled to Sn-I stretching
	v'_3	170.82	MA librational mode
	v'_4	247.12	MA torsional mode
	v'_5	299.42	MA torsional mode
	v'_6	344.26	MA torsional mode

interfaces appear blurred because structure is usually grown at low-order zone axes, which limits the spatial resolution and interpretability of the results. Therefore, the NBED technique is becoming increasingly favored over CBED. The technique involves forming a spot pattern from a small area on the sample. First, a pattern is taken from a reference area of the sample (typically the substrate), and the spot positions are determined. Patterns are then taken successively from different areas, and the shifts in spot positions are used to determine the deformation tensor at each of probe position. It is sensitive to atomic column bending, which may affect the accuracy of results.

Furthermore, the utilization of a HRTEM image with micro-area diffraction pattern enables the quantification of strain via the measurement of crystal plane spacing. For instance, Rothmann *et al.*[58] have employed TEM to observe the types and distributions of misfit dislocations (MDs), which lead to non-uniform strain field. With respect to epitaxially grown materials, TEM is employed to monitor strain relaxation in the epilayer. While perfectly grown epitaxial layers lack interfacial defects, uncontrolled strain relaxation produces numerous defects, which can be visualized by TEM. Conversely, controlled strain relaxation of the epilayer results in a uniform interfacial misfit dislocation array. As depicted in Figure 6a, b, a misfit dislocation array at the GaSb/GaAs interface is observed, and uniform IMF arrays are evident in both samples, denoted by black arrows. The distance between two adjacent MDs in GaSb/GaAs is measured to be 5.6 nm, while that in InSb/GaAs is 3.2 nm, implying that IMF arrays are successfully formed at the III-Sb/GaAs interfaces.[59] Additionally, Zhang *et al.*[60] utilized HRTEM to confirm the presence of a single layer of nanosheets. Figure 6c depicts the HRTEM images of the P-Nb_2CT_x MXene nanosheets, with lattice parameters of 0.27 nm corresponding to the (042) plane of Nb_2C. Furthermore, the corresponding selected area electron diffraction (SAED) patterns of the P-Nb_2CT_x MXene nanosheets are shown in the

DOI: 10.54227/elab.20230004

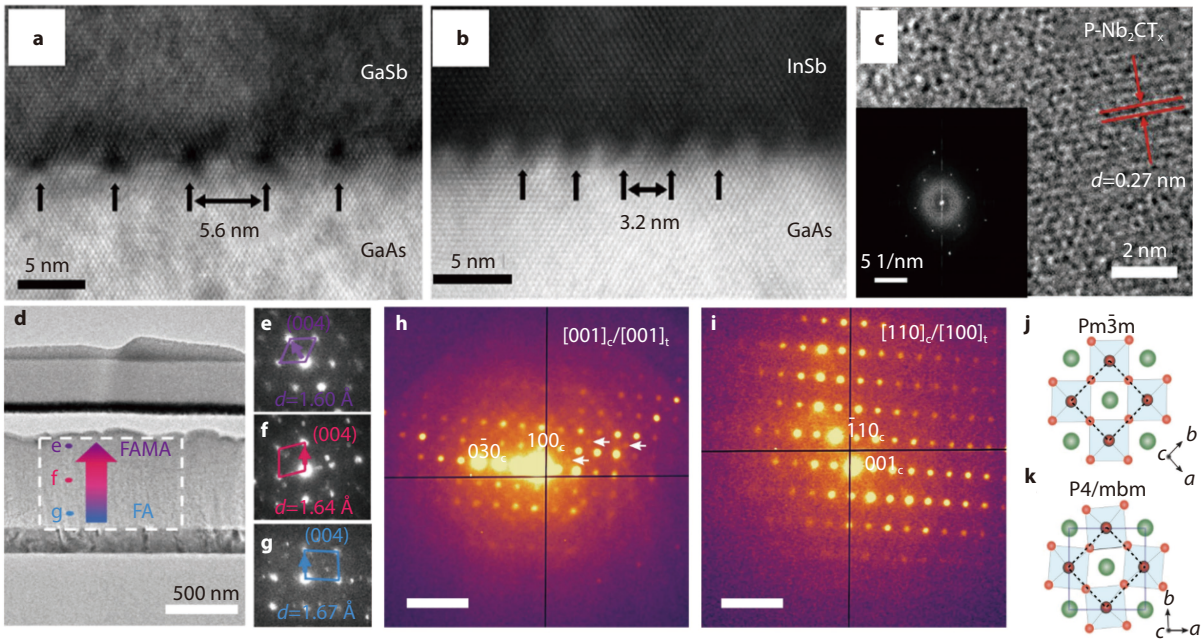

Fig. 6 Cross-sectional TEM image of the interfacial misfit dislocations for **a** GaSb and **b** InSb grown on GaAs samples with (2×8) Sb reconstruction prior to growth, respectively.[59] Copyright 2017, Applied Surface Science. **c** HRTEM image of P-Nb_2CT_x MXene nanosheet. The inset image shows the corresponding selected area electron diffraction (SAED) pattern.[60] Copyright 2022, Advanced Functional Materials. **d** The cross-sectional TEM image of device. **e,f,g** The NBED patterns ([100] zone axis and TEM specimens is FIBed), corresponding with e-f-g point in **d**, confirming the FAMA hybrid perovskite phase structure transform to nearly pure FA phase from the surface to the bottom of perovskite film according to the larger quadrangle.[35] Copyright 2019, Nature Communications. **h** SED patterns of triple/cation perovskite corresponding to $[001]_c$ zone axis demonstrating the presence of superlattice reflections (white arrows), which are normally forbidden in a cubic *Pm3m* structure, often assumed for halide perovskite materials, as shown in **i**. Analyzing SED pattern near $[110]_c$ zone axis in **j** allows to conclude that perovskite has a *P4/mbm* structure shown in **k**. Scale bar is 0.5 $Å^{-1}$.[62] Copyright 2021, Science.

insert of Figure 6c, which implies the hexagonal structure of the P-Nb_2CT_x MXene nanosheets. The thickness of these Nb_2CT_x MXenes is approximately 2 nm, which confirm the successful preparation of single layer nanosheets. Moreover, Chen *et al.*[35] obtained HRTEM images with microarea diffraction patterns to examine three distinct regions with varying depths (Figure 6d-g). As shown in Figure 6e-g, the lattice parameters of (004) planes were measured to be 1.60, 1.64, and 1.67 Å for three individual areas, respectively. This finding suggests the vertical evolution of lattice structure in mixed perovskite polycrystalline thin films, where the lattice constant increases from the surface to the bottom. Finally, the recently developed technique of DFEH enables the mapping of strain by directly measuring the phase of diffracted beams. Analysis of the simple diffraction conditions relevant to DFEH has allowed for the determination of an analytical formula for the projection rule and the averaging of strain over different depths in the thin film.

SED

SED, a 4D-STEM technique, relies on acquiring of a 2D transmission electron diffraction pattern at every probe position as a focused electron probe scans across the specimen in a 2D scan.[61] Employing SED microscopy enables the resolution of micro- and nano-scale strains. The technique yields nanoscale spatially-resolved diffraction patterns to characterize local changes in *d*-spacing, grain orientation, and strain (Figure 6h-k).[62] For example, in these SED (Figure 6h), scans with spatial resolution of 5 nm (extracted from individual grains 50 to 200 nm in size), very faint reflections, forbidden from appearing in the *Pm3̄m* (Figure 6j), space group, were visible (Figure 6h, white arrows). When combined with other analytical techniques, SED measurements may be used to unveil the connection between perovskite's strain, chemical composition, and photoelectric properties.[63]

EBSD

EBSD allows crystallographic information to be obtained from small volumes of a material in a SEM, which provides versatility in mapping orientation, crystal type, and perfection over a wide range of step sizes. EBSD maps are formed by moving a focused probe of electrons point-by-point across a grid of positions on the surface of a bulk sample. At each point, some electrons backscattered from the sample are collected by a detector comprising a scintillator screen coupled generally by a lens or sometimes by a fiber optic bundle to a photon sensitive imaging detector for an electron backscatter diffraction pattern. Ginger *et al.*[37] used EBSD to measure local crystal orientation in halide perovskite films treated with solution (Figure 7a). Based on SEM morphology alone, the black arrow in the SEM image in Figure 7b would be assigned as going across a single "grain boundary". However, from the corresponding inverse pole figure (IPF) map (Figure 7d) they noted that the film actually possesses 3 distinct boundaries separating 4 different local crystal orientation changes along the same arrow. Figure 7d depicts the changes in the local crystal orientation occurring across the arrow shown in Figure 7b-c. Then they used the plot of grain orientation spread

DOI: 10.54227/elab.20230004

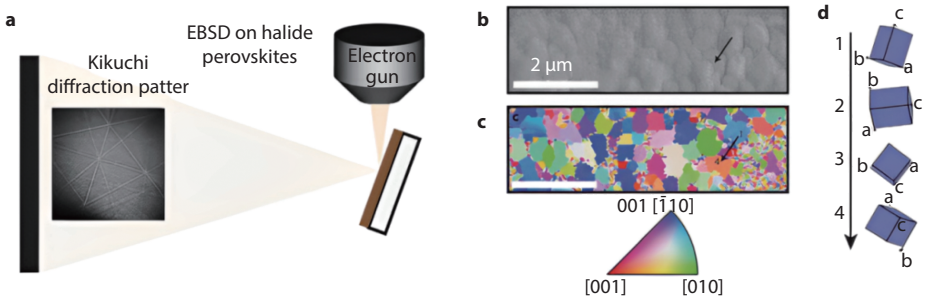

Fig. 7 **a** Schematics of EBSD measurement on $CH_3NH_3PbI_3$ thin films. **b** Top-view SEM image and **c** IPF map generated from EBSD of $CH_3NH_3PbI_3$ thin film with IPF color key. **d** Depiction of changes in local crystal orientation along the black arrow in **b** and **c** as viewed normal to the sample.[37] Copyright 2019, Joule.

(GOS) to show grain-to-grain heterogeneity in average local misorientation in $CH_3NH_3PbI_3$ perovskite film, which generated using EBSD and IPF color key. Higher GOS values indicate grains with higher strain, and lower GOS values indicate grains with lower strain. The measured local crystal misorientation confirmed the existence of local strain.

PFM

PFM is an atomic force microscopy (AFM) mode, which is used to detect electromechanical material properties on the nanometer scale. A conductive tip is used to detect the response of a sample to an AC voltage. Yalcinkaya *et al.*[64] prepared several batches of $MAPbI_3$ films with precursor ratios between 9:1 and 6:4 and subsequently investigated the topography and the lateral piezoresponse by PFM (Figure 8a-d). The lateral PFM amplitude images showed the familiar striped ferroelastic domain structure (Figure 8c-d), the films prepared with the 6:4 precursor ratio showed a less dense domain structure (Figure 8d) compared with $MAPbI_3$ films with 9:1 $Pb(Ac)_2/PbCl_2$ ratio (Figure 8c). In particular, they found an increased width for the ferroelastic twin domains by increasing $PbCl_2$ dosage. The most obvious effect of the precursor ratio change is an increase in average grain size from 2.04 ± 0.11 μm for the 9:1 $Pb(Ac)_2/PbCl_2$ ratio to 3.9 ± 0.3 μm for the 6:4 $Pb(Ac)_2/PbCl_2$ ratio (Figure 8e). The decrease in grain size is attributed to the decreased Cl or MACl content when the content of lead chloride is reduced, which accelerates the crystallization of perovskite and leads to smaller grain size. Figure 8f showed the average ferroelastic twin domain width gathered from various areas of the samples. The distances between the high-amplitude and low-amplitude areas revealed an average domain width of 137±10 nm for the $MAPbI_3$ film with 9: 1 as well as 560±90 nm for the 6:4 Pb $(Ac)_2/PbCl_2$ ratio (Figure 8f), respectively. As twin domains are purely strain released, it seems obvious from the changing domain pattern that the strain in the films is influenced by different $Pb(Ac)_2/PbCl_2$ ratios. Strelcov *et al.*[43] demonstrated that external strain could alter the domain structure, the stripe-shaped domains evolved into larger areas upon increasing the strain within the $MAPbI_3$ films. Their work demonstrates how strain is generated in halide perovskite films to form "stripe-shaped" domains.

Impacts of strain

Strains effects on perovskite films are known to cause a range of diverse impacts, including alterations to their band structure, defect properties, crystallinity, and stability. In this section, we will discuss these implications in detail.

Band structure

Ascertained in the preceding discussion, perovskite strain gradients can be deduced from XRD pattern and Raman spectroscopy. For instance, Chen *et al.*[16] investigated the α-$FAPbI_3$ crystal structure under increased compressive strain (from 0% to -2.4%) and discovered its reduced bandgap and increased hole mobility using Raman spectroscopy and photoluminescence (PL) spectra. The stretching of lead-iodine bonds results in a peak at approximately 136 cm^{-1} in the Raman spectra, which increased in intensity and broadened as the compressive strain increased. A slight pressure of 0.3 GPa caused the absorption edge of compressed perovskite to experience a considerable red-shift, indicating a reduction in bandgap. Notably, the narrowed bandgap caused an increase in carrier lifetime by 70%~100%.[65] Compression alters the lattice structure of $MAPbI_3$, resulting in a rethinking of the boundary conditions for electronic wave functions. The adjustment of the optoelectronic properties is primarily due to the narrowing of the bandgap, which is determined by the variation of the conduction band minimum (CBM) and valence band maximum (VBM). As illustrated in Figure 9a, compressive pressure of 3 GPa pushes the VBM of $FA_{0.75}Cs_{0.25}PbI_3$ upward by 0.2 eV, while the CBM upward by only 0.08 eV.[9] Thus, both CBM and VBM shift to higher energy under compressive, but VBM moves to a more significant extent than CBM. Consequently, the application of compressive strain shifts the VBM of perovskites to a higher energy level, which is beneficial for better energy level alignment between the perovskite film and the HTL, as well as reducing the perovskite's bandgap.[9]

It has also been reported that strain affects the carrier mobility and lifetime. Chen *et al.*[35] used depth-dependent GIXRD measurements to reveal the gradient evolution of residual strain in the vertical direction of mixed halide perovskite film, and performed first-principles calculations to explain the underlying mechanism (Figure 9b). They found that the bandgap of the films increased as the strain changed from compression, zero-strain, to tension, and the carrier lifetime was also affected by strain. Kong *et al.*[65] investigated the impacts of pressure on carrier lifetime (τ) using in-situ high pressure TRPL measurements for hybrid perovskites (Figure 9c). Compared with the values of the mean carrier life-

DOI: 10.54227/elab.20230004

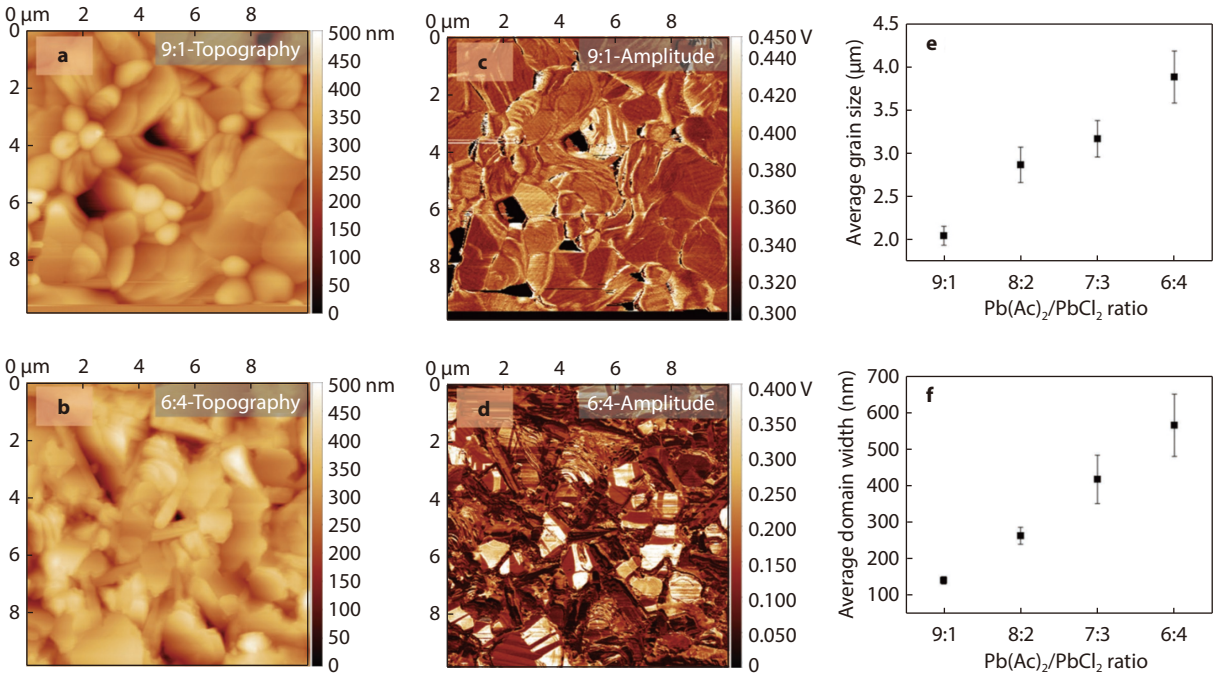

Fig. 8 Topography and PFM amplitude images of $MAPbI_3$ thin films with $Pb(Ac)_2/PbCl_2$ ratios of **a, c** 9:1, and **b, d** 6:4. **e** Average grain size and **f** domain width profiles of $MAPbI_3$ thin films with different $Pb(Ac)_2/PbCl_2$ ratios.[64] Copyright 2022, Advanced Energy Materials.

time measured at 1 atm, a dramatic increases of 70% and 100% was observed at 0.3 GPa for single crystals and polycrystals, respectively, which is consistent with the pressure of an obvious red shift of the absorption edge of the compressed perovskite. The induced-valence bands bending of perovskite films inevitably affect the interfacial hole dynamics. Thus, reducing the strain gradient of perovskite film via strain engineering is an effective method to improve hole carrier extraction and transport.

Chen *et al.*[16] calculated the electron effective mass (m_e^*), and hole effective mass (m_h^*) and three typical electronic band structures under different strains, as shown in Figure 9d. The electron effective mass (m_e^*) remained relatively stable with the change in strain, while the hole effective mass (m_h^*) decreased with increasing compressive strain. The Hall-effect carrier mobility of the α-$FAPbI_3$ film was measured by subjecting it to a strain ranging from 0% to −2.4%, as illustrated in Figure 9e. The highest hole mobility on a $MAPbCl_{0.60}Br_{2.40}$ substrate was achieved at −1.2% strain. However, further higher strain level could cause a higher dislocation density and therefore a significant decrease in the hole mobility. To validate the Hall mobility results, the carrier mobility was also evaluated using the time-of-flight technique (TOF), as depicted in Figure 9f. The carrier transit time revealed that the perovskite film exhibited the shortest value at −1.2% strain. The carrier mobility can be calculated using the formula:

$$\mu = \frac{d^2}{Vt}$$

where μ is the calculated carrier mobility, d is the thickness, V is the applied voltage, and t is the measured carrier transit time. By plotting the calculated carrier mobility as a function of the applied strain (Figure 9g), they observed a similar trend to that given by the Hall effect. The researchers noted that the absolute mobility values from the TOF and Hall effect measurements are different, as these device measurements tend to be influenced by the quality and type of electrical contact.[5]

Defect properties

The classification of defects in perovskites is based on the position of their electronic transition levels within the band gap. Defect trap states can be classified as "deep" or "shallow" depending on their relative positions to the CBM or VBM.[66] Deger *et al.*[67] found that strain not only controls the formation of defects but also their transition levels in the band gap. They varied the crystal strain of $CsPbI_3$, $FAPbI_3$ and $MAPbI_3$ from −2% (compressive) to 2% (tensile) with point defects of $I_{A\text{-site}}$, I_{Pb}, $V_{A\text{-site}}$, V_I, V_{Pb}, and I_i. Charged point defects has been shown to be efficient non-radiative recombination centers, which can limit the open-circuit voltage (V_{oc}) of a solar cell.[19] They demonstrated that a compressive strain in $CsPbI_3$ stabilized the defect formation energy (DFE) of V_{Cs} up to 7% (Figure 10a). Interestingly, electron donation causes a significant contraction of the center of a defected unit cell in the *x*-direction, resulting in an increase in DFE due to compressive strain. Moreover, the DFEs of V_{Cs}, I_{Cs}, V_{Pb} and I_i decreased for compressive strain, resulting in an expansion along the *x*-axis. This means that lattice strain can restore the distortion where the defect is located. Furthermore, lattice strain has an effect on the transition levels (Figure 10b-c). In particular, a tensile strain applied to the $FAPbI_3$ leads to the transformation of deep FA antisiite (I_{FA}) defects into shallow ones. Transition levels for the point defects of $I_{A\text{-site}}$, I_{Pb}, $V_{A\text{-site}}$, V_I, V_{Pb}, and I_i in $FAPbI_3$ and $MAPbI_3$ are shown in Figure 10e-f. These results indicate that strain can control the transition level of a defect in the bandgap and even deep defects can be transformed into shallow ones via strain.

Figure 10d reveals that the Goldschmidt tolerance factor (*t*)

DOI: 10.54227/elab.20230004

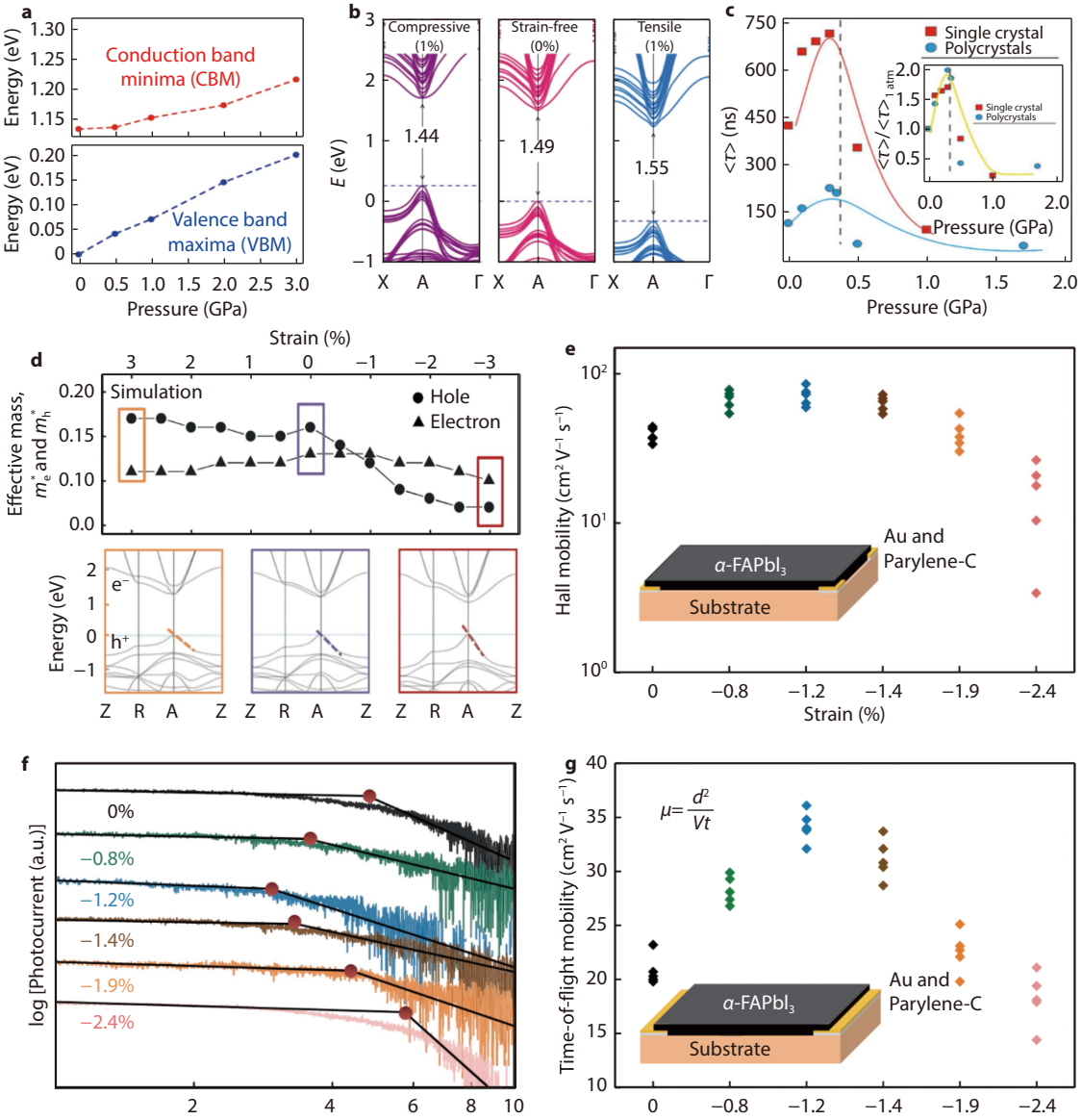

Fig. 9 **a** Modification in energy of CBM and VBM.[9] Copyright 2021, National Science Review. **b** Calculated band structures under biaxial tensile, zero, and compressive strains from first-principle density functional theory (DFT)-based approaches.[35] Copyright 2019, Nature Communications. The band structure alignment is made by using the vacuum energy level as reference. **c** Pressure dependence of the mean carrier lifetime, for both $MAPbI_3$ single-crystal and polycrystal samples. Peak values in carrier lifetimes of $MAPbI_3$ were observed at 0.3 GPa. (c Inset)[65] Copyright 2016, Proceedings of the National Academy of Sciences. **d** Calculated effective masses of the carriers at different strains, and electronic band structures under three strain levels (3%, 0% and −3%). **e** Hole mobilities by Hall effect measurements. **f** Transient photocurrent curves of the epitaxial α-$FAPbI_3$ under different strains. **g** Plots of calculated carrier mobilities as a function of the strain magnitudes.[16] Copyright 2020, Nature.

of the three perovskites, namely $CsPbI_3$, $MAPbI_3$ and $FAPbI_3$ are 0.89,[27] 0.91,[68] and 0.99,[68] respectively. Remarkably, $FAPbI_3$ exhibits the highest value, which is very close to the hexagonal phase transition area. This result implies that crystal distortions exert a more pronounced influence on the formation of defects in $FAPbI_3$.[67] Under compressive strain, the value of *t* decreases to the stable cubic region, thereby increasing the formation energy of defects. Xue *et al.*[15] have likewise reported that tensile strain decreases the formation energy of defects, while compressive strain increases it, as compared to the strain-free perovskites. Consequently, defects are more prone to form under tensile strain,[69] leading to an elevated rate of non-radiative recombination.[9]

Stability

Ion migration

The impact of strain on ion migration is closely connected to the accelerated perovskite degradation caused by strain. Huang *et al.*[13] conducted a study on the activation energy (E_a) for ion migration in $MAPbI_3$ films under both dark and illumination conditions (Figure 11). For the convex, flat, and concave $MAPbI_3$ films, the E_a values for ion migration in the dark were 0.29 eV, 0.39 eV, and 0.53 eV. Under white light illumina-

DOI: 10.54227/elab.20230004

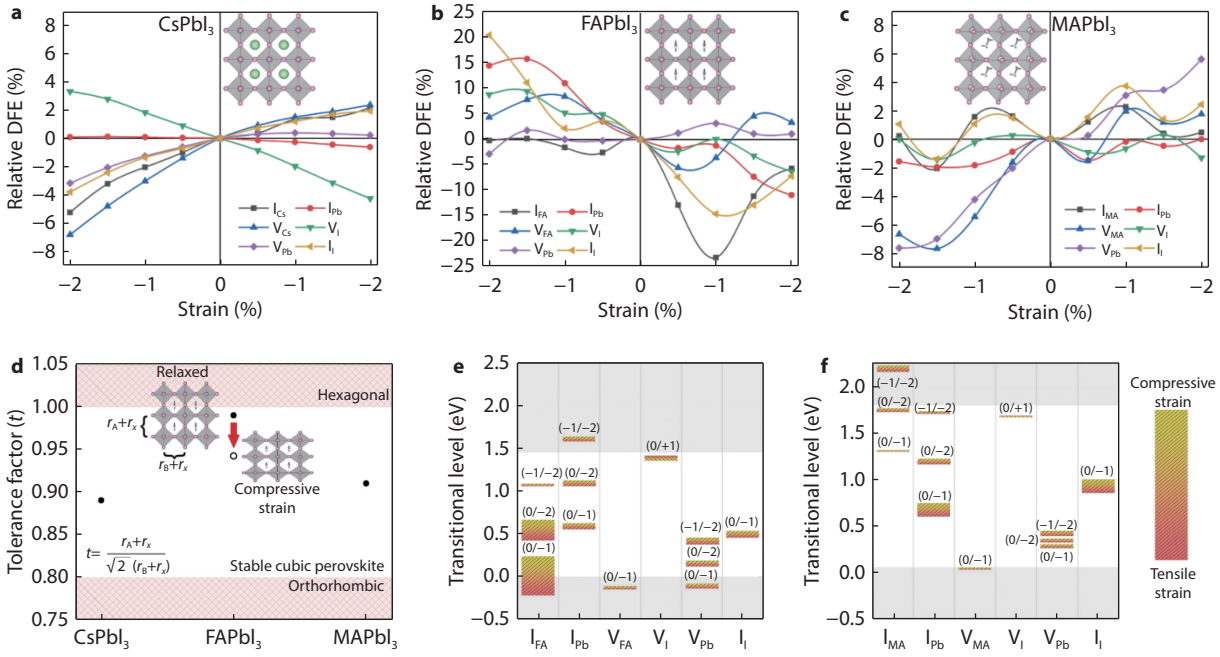

Fig. 10 The dependence of the defect formation energies (in eV) on the lattice strain and defect formation energy of the perovskites for different growth conditions. The relative DFE with respect to the strain for selected neutral intrinsic defects (I_A, I_{Pb}, V_A, V_I, V_{Pb}, and I_i) in **a** $CsPbI_3$, **b** $FAPbI_3$, and **c** $MAPbI_3$ perovskites under moderate conditions. The negative percentage value indicates a compressive strain while the positive percentage value refers to a tensile strain along the out-of-plane direction throughout the study. **d** Schematic representation of strain-induced tolerance factor adjustment of $FAPbI_3$. Herein, r_A, r_B, and r_X represent the radii of A-site molecule, B-site metal, and X-site halide in ABX_3 perovskites, respectively. In addition, r_A+r_X is a space-diagonal length. The change in the tolerance factor of $FAPbI_3$ is enlarged to show the influence of the strain. The charge transition energy levels of selected intrinsic defects in **e** $FAPbI_3$, and **f** $MAPbI_3$. The influence of lattice strain on the transition levels is shown by the color gradient. The strain is varied from −2% (compressive) to 2% (tensile).[67] Copyright 2022, Nano Research.

tion at an intensity of 25 mW cm^{-2}, these values decreased to 0.046 eV, 0.074 eV, and 0.083 eV, respectively. The highest E_a value was observed in the concave perovskite film, suggesting suppressed ion migration. Larger strain on perovskite films was found to result in lower E_a for ion migration, under both dark and illumination conditions (Figure 11). Muscarella *et al.*[70] provided an explanation for the process of phase segregation at atomic scale, nanoscale and macroscale. Their findings indicate that halide migration within the perovskite lattice leads to additional instability for the demixing of halides into separate phases. They also demonstrated that the E_a for halide ion migration was increased in compressed films, while phase segregation was suppressed when tensile strain was compensated by compressive strain.

Phase stability

Investigating the correlation between strain and phase stability of halide perovskite films is of paramount importance. The structural stability of ABX_3 perovskite can be evaluated by *t*, and perovskite structures are formed when *t* falls within the range of 0.71 to 1.[71] According to this theoretical framework, FA^+ cation is too large (t = 0.99)[68] for the perovskite structure, leading to the formation of the nonphotoactive yellow δ phase at room temperature. In contrast, the MA-perovskite, with an appropriate *t* value of 0.91,[68] retains a black, photoactive tetragonal or cubic structure at operating temperatures ranging from −15 to 65 °C (Figure 12a).[72] Owing to the internal lattice strain and low entropy[26,73] α-$FAPbI_3$ crystals are metastable at room temperature and can rapidly transform into the nonphotoactive δ-$FAPbI_3$ phase within 24 hours.[74] The internal tensile strain in α-$FAPbI_3$ facilitates the formation of vacancies, which is regarded as the driving factor behind the α-to-δ phase transition.[8]

Steele *et al.*[12] utilized an ab initio thermodynamic model to investigate the energy change from γ-$CsPbI_3$ to δ-$CsPbI_3$ under different strain conditions (Figure 12b). The transition from γ to δ phase in free-standing $CsPbI_3$ crystals occurs due to the relatively lower thermal energy of the unstrained yellow phase compared to that of the unstrained black phase. However, biaxial strain causes energy loss in both phases, thus suppressing the transition from γ phase to δ phase and reducing the energy difference. This provides an explanation as to why the application of biaxial strain increases the phase stability of $CsPbI_3$. Another theory holds that strain collaborates with surface formation energy to enhance the stability of $CsPbI_3$ by reducing the crystal size. By decreasing the crystal size, surface energy-driven phase change can be restrained, thus offering a promising strategy for addressing the metastable polymorphism problem. The variation in surface formation energy of γ- and δ-$CsPbI_3$ can be determined as a function of compressive strain (Figure 12c).[75] The difference in surface formation energy indicates that α-$CsPbI_3$ stabilizes faster under compressive strain, as it has a lower surface formation energy than δ-phase $CsPbI_3$. Ma *et al.*[75] systematically fabricated nanoporous anodized aluminum oxide (AAO) templates with pore sizes ranging from 30 to 112 nm. These tem-

DOI: 10.54227/elab.20230004

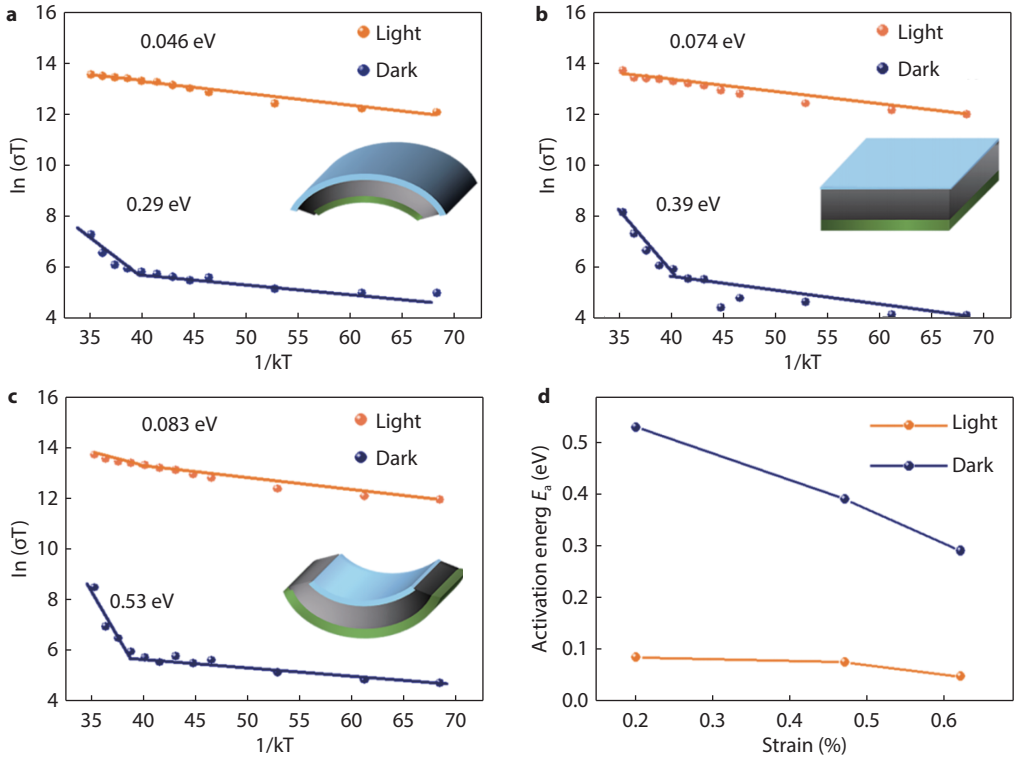

Fig. 11 Ion migration properties of $MAPbI_3$ films at different strains. **a-c** The temperature-dependent conductivity of **a** the convex film, **b** the flat film, and **c** the concave film. Inset: Schematic diagram of the samples. **d** Variation of the activation energy of ion migration as a function of the strain in the $MAPbI_3$ films.[13] Copyright 2017, Science Advances.

plates were utilized as a host matrix for the infiltration of $CsPbI_3$ precursor solutions. The growth of $CsPbI_3$ crystals inside AAO templates with pore sizes of 41 nm was found to be hampered by the pore walls, leading to anisotropic microstrain perpendicular to the pore walls (Figure 12d). This microstrain induced lattice distortion and enhanced the phase stability of the α-phase $CsPbI_3$ under compressive strain. In the case of $CsPbI_3$ grown in a 112 nm pore AAO template, the α-phase $CsPbI_3$ crystal structure grew rapidly without the compressive stress imposed by the pore walls. This resulted in the rapid conversion of the metastable cubic perovskite structure to an orthorhombic nonperovskite structure upon annealing (Figure 12e). Wu *et al.*[76] employed bulky organic ligands as organic terminal groups (OTGs) to enhance the phase stability of $CsPbI_3$ perovskite by impeding lattice distortion induced by moisture or polar solvents (Figure 12f). The steric hindrance provided by OTGs effectively prevents the formation of lattice distortion, thereby inhibiting the phase transition of $CsPbI_3$.

Perovskite film and device stability

The impacts of strain on perovskite film and device stability are significant. Xue *et al.*[15] found that the photostability of PSC under continuous one sun illumination and maximum power point (MPP) conditions varied greatly with strain (Figure 13a). The compressive-strained and unstrained devices maintained 95% and 81% of their initial PCEs after continuous MPP operation for 60 h, whereas the tensile-strained device maintained only 50% of its initial PCE after tens of hours. They further tested the thermal stability of PSCs under continuous heating at 85 °C. The stability evolution was similar to that under MPP condition (Figure 13b). They attributed the PCE loss of the tensile-strain device to the phase degradation into Br-rich and I-rich perovskite phases, and subsequent transition of I-rich phase from photoactive to non-photoactive phase (α to δ). Meng *et al.*[77] evaluated the photostability of a PSC under continuous 1 sun illumination in a N_2-filled chamber. As shown in Figure 13c, the PCE of the control device dropped to 22% of its initial value after 1000 h, however the device with a strain-released perovskite film was much more stable, maintaining 82% of its initial PCE under the same testing conditions. As a contrast, the best device showed an excellent long-term performance and sustained over 93% of its original efficiency in the dark (Figure 13d). The difference in device stability is assigned to strain-induced defects at the SnO_2 interface, which can trigger ionic migration and phase separation and to accelerate degradation. Huang *et al.*[13] conducted control experiments on convex, flat and concave perovskite films, as shown in Figure 13e-f, to study the effects of different strain conditions on perovskite films, and the lattice strain in those three films were approximately 0.62, 0.47 and 0.2%, respectively. In contrast to the films with the smallest strain, which usually stayed black after 500 hours of illumination, the films with the larger lattice strain had large area that became yellow, which was typically a characteristic of the decomposition of $MAPbI_3$ into PbI_2 (Figure 13e). The XRD pattern depicted in Figure 13f supported the findings.

DOI: 10.54227/elab.20230004

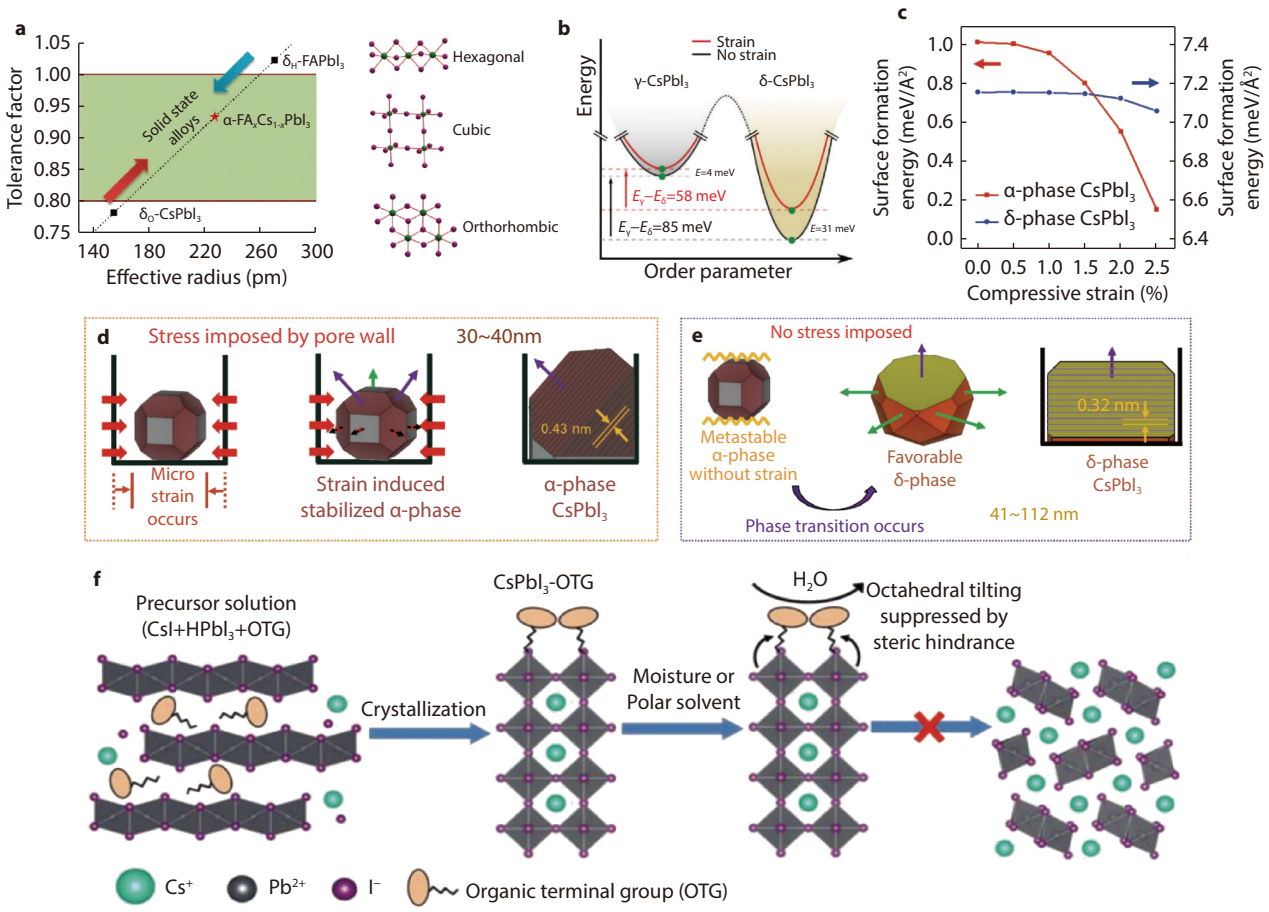

Fig. 12 **a** Correlations between tolerance factor and crystal structure of perovskite materials.[72] Copyright 2016, Chemistry of Materials. **b** The schematic diagram for the relative stability of the black phase and yellow phase with and without biaxial strain.[12] Copyright 2019, Science. **c** Dependence of surface formation energy on the imposed compressive strain obtained through a theoretical calculation.[75] Schematic describing the polycrystalline growth mechanism of **d** α-phase $CsPbI_3$ perovskite in 41 nm pore-sized anodized aluminum oxide (AAO) template and **e** δ-phase $CsPbI_3$ perovskite in 112 nm pore sized AAO template. Copyright 2019, Small. **f** Mechanism of the OTG-induced phase stabilization of $CsPbI_3$ perovskite.[76] Copyright 2019, Advanced Materials.

Strain regulation strategies

Compositional engineering

The compositional engineering of perovskite halide is a widespresd strategy for mitigating strain in halide perovskite films. A preferred approach involves the incorporation of foreign ions into the host perovskite lattice.

Cation/anion doping

The influence of A-site cation doping on the strain regulation in perovskites has been the subject of extensive investigation. For example, Hayase *et al.*[78] explored the impact of A-site cations on the lattice strain of $FA_{0.75}MA_{0.25}SnI_3$ perovskite using XRD patterns. To form $Q_{0.1}(FA_{0.75}MA_{0.25})_{0.9}SnI_3$ films, a range of A-site cations with different sizes were employed, including Na^+, K^+, Cs^+, ethyl ammonium$^+$ (EA^+) and butylammonium$^+$ (BA^+). The results indicated a gradual reduction in the lattice strain of Sn-based perovskite as the tolerance factor getting closer to 1 due to the stronger formation tendency of the cubic crystal structure (Figure 14a). As the lattice strain decreased, the efficiency of Sn-based PSC increased. Among these, $EA_{0.1}(FA_{0.75}MA_{0.25})_{0.9}SnI_3$, with the lowest lattice strain, achieved the highest PCE of 5.41%. However, these lattice strains could impede carrier mobility and decrease device efficiency. The storage-induced relaxation of the lattice strain, on the other hand, enhanced the efficiency of the $FA_{0.75}MA_{0.25}Sn_{1-x}Ge_xI_3$ PSCs from 6.42 to 7.60%.

Kim *et al.*[25] employed dual substitution of FA^+ sites with methylene diammonium (MDA^{2+}) and Cs^+ in the same molar ratio to relax the lattice strain. Substituting only MDA^{2+} cations with a larger ionic radius, or Cs^+ with a smaller ionic radius, than FA^+ can distort Pb-I-Pb bonds by tilting the PbI_6 octahedron. By introducing larger ions (MDA^{2+}) and smaller ions (Cs^+) together, the local tensile and compressive strain in the perovskite lattice were reduced. The addition of both MDA^{2+} and Cs^+ cations to alloyed $FAPbI_3$ at a 0.03 mol fraction was found to effectively reduce lattice strain and nonradiative carrier recombination in PSCs, resulting in certified efficiencies of 24.4 and 21.6% for small and large (1 cm by 1 cm) cells, respectively. Chen *et al.*[79] explored the relaxation of residual strain in hybrid perovskite films by incorporating different A-site cations, such as large phenethyl ammonium (PEA^+) and octyl ammonium (OA^+). The incorporation of organic A-site cations is known to modify interfacial interaction, and

DOI: 10.54227/elab.20230004

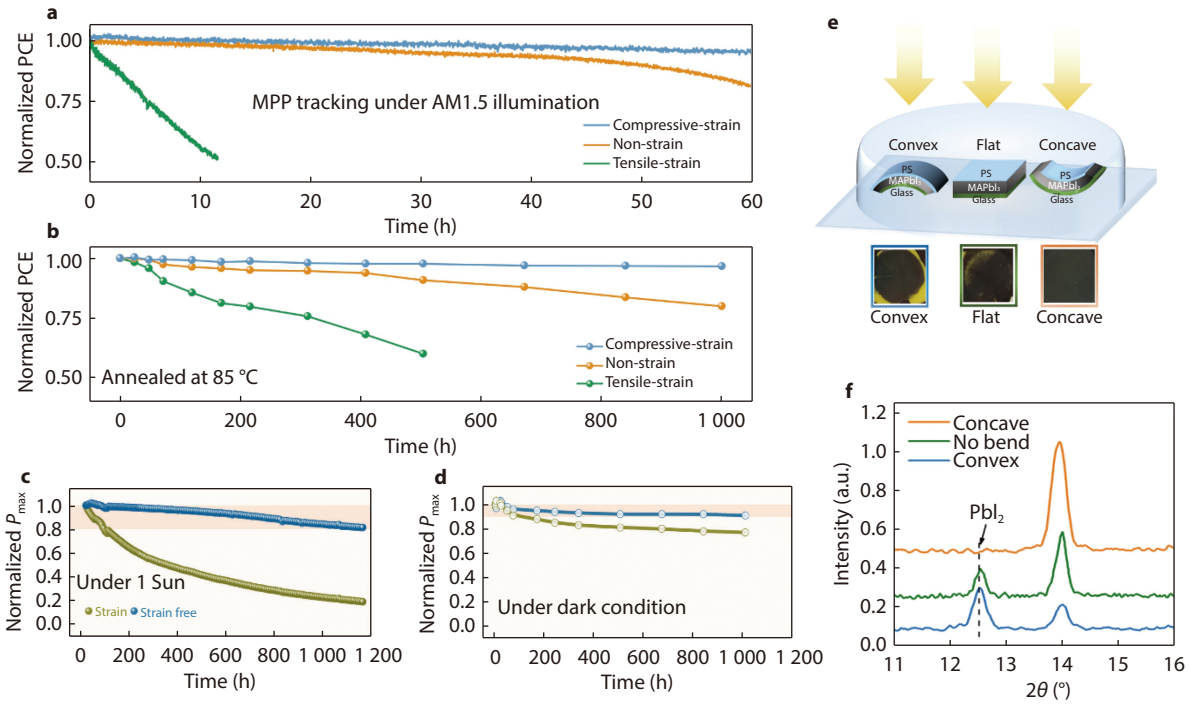

Fig. 13 **a** Evolution of normalized PCEs under MPP tracking and continuous simulated solar illumination (100 mW cm^{-2}). **b** Evolution of normalized PCEs of PSCs kept at 85 °C in a nitrogen atmosphere. The device stability tests under continuous white LED illumination.[15] Copyright 2020, Nature Communications. **c** The light intensity was adjusted in a way that the J_{sc} matched the ones under a solar simulator. **d** The device stability tests in the dark.[77] Copyright 2022, Joule. Strain impact on perovskite film stability. **e** Schematic diagram for the experimental setup of the films with different strains and photographs of the films with different strains after 500 h illumination. **f** Out-of-plane XRD of the three films in **a**.[13] Copyright 2017, Science Advances.

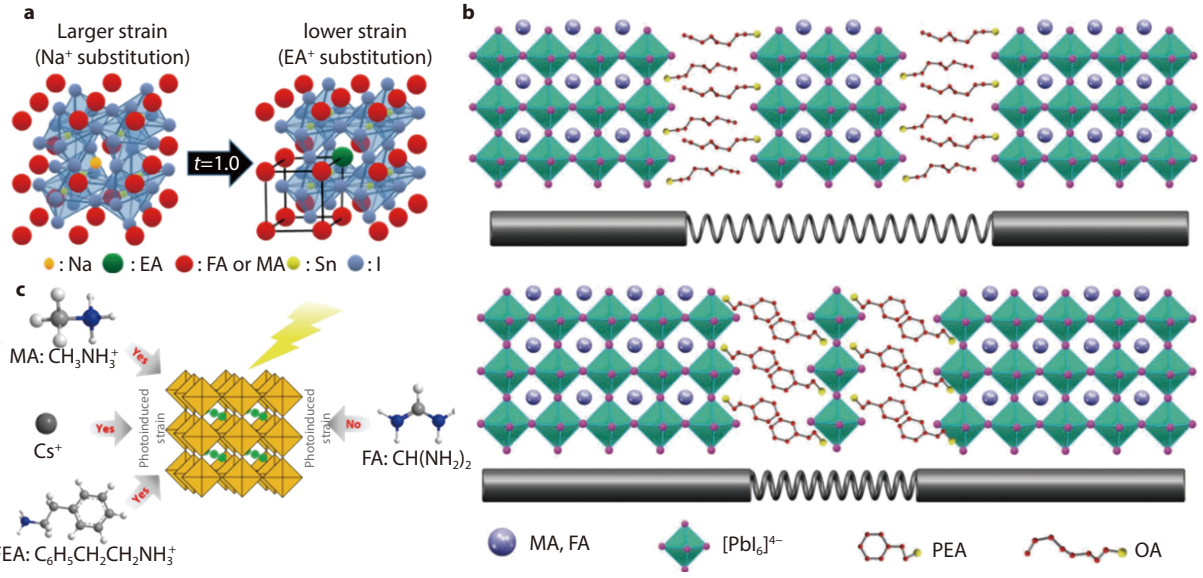

Fig. 14 **a** Schematic diagram for the adjustment of A-site in $FA_{0.75}MA_{0.25}SnI_3$ perovskite to reduce lattice strain.[78] Copyright 2019, ACS Applied Materials & Interfaces. **b** Schematic describing the residual stress relaxation with soft and stiff structural subunits.[79] Copyright 2019, Advanced Materials. **c** Schematic diagram for the adjustment of A-site in perovskite to reduce lattice strain.[80] Copyright 2019, Journal of Materials Chemistry A.

Figure 14b illustrates the in-depth mechanism of residual strain relaxation through OA/PEA treatment. The incorporation of large organic cations results in the formation of 2D perovskite components that mainly reside at the surface of the perovskite films to construct "soft" structural subunits. These subunits containing OA^+ are "softer" than PEA^+ due to the greater flexibility of OA^+ compared to PEA^+ with a stiff benzene ring. This property helps retain the microstructure of

DOI: 10.54227/elab.20230004

the polycrystalline film to reduce the residual strain during conventional annealing.

Lu *et al*.[80] demonstrated that introducing guanidinium cations (GA^+) cations could significantly improve the structural stability and device performance of a $CsPbI_2Br$ PSC. By occupying the substitutional sites of Cs, GA can effectively alleviate the lattice strain induced by the comparatively smaller Cs cations. Moreover, GA can establish strong hydrogen bonds with the neighboring $[PbI_6]^{4-}$ octahedral building blocks, thus hindering the transformation from the cubic phase to the orthorhombic phase. Ovchinnikova *et al*.[44] found that the A-site cation plays a crucial role in light-induced lattice strain in perovskites. Among the four cations (MA, FA, Cs, and PEA) studied in their work, FA was different from the other three cations because FA-based perovskites ($FAPbI_3$) did not exhibit lattice expansion upon illumination (Figure 14c). The stronger hydrogen-bonding interaction for FA, due to its two NH_2 groups, could result in a more rigid response. DFT calculations demonstrates that the ionization energy for FA is much larger than that of PEA, and the estimated value of charge transfer integral is 2 orders of magnitude larger, indicating that the formation of holes on FA is more difficult and those holes, once formed, will move quickly compared with PEA, pointing to $FAPbI_3$ having the least lattice distortion and PEA_2PbI_4 having the largest. This special aspect of FA^+ is the potential mechanism behind the most stable PSCs using FA^+ as majority cation. In contrast, all the perovskite based on these four cations exhibited a lattice expansion upon heating.

The doping of A- and X-site cation could also regulate strain in the perovskite structure. Seok *et al*.[81] reported highly efficient and stable PSCs fabricated with α-$FAPbI_3$ by incorporating a small amount of methylene diammonium dichloride ($MDACl_2$). A small amount of Cl^- substitution can reduce the lattice strain of $FAPbI_3$ and suppress defect formation. Also, MDA^{2+} cations could ease the insertion of smaller Cl^- ions into the interstitial spaces. Smaller Cl^- ions substituted at the I sites of $FAPbI_3$ contribute to phase stabilization by reducing the lattice strain of the α-phase.[8] Finally, they achieved a certified PCE of 23.73% with short-circuit current density (J_{sc}) of 26.1 mA cm^{-2}. In addition, the doping of B- and X-site cations could also regulate strain in the perovskite structure. Saidaminov et al.[8] chosed B/X isovalent candidates (B: Pb^{2+}, Ba^{2+}, Sr^{2+}, Ca^{2+}, Hg^{2+}, Cd^{2+}, Zn^{2+}; X: I^-, Br^-, Cl^-) to relax the remaining lattice strain on B/X sites to maximize further the formation energy of the most abundant defect without introducing electronic traps. Specially, DFT calculations showed that when I was partially replaced by Cl, the Pb–X bond lengths decreased, as did the Pb–X–Pb distortion angles, and the I vacancy formation is suppressed by≥0.3 eV. Finally, they found suppressing atomic vacancies via incorporation of Cd and Cl within the CsMAFA lattice further enhances the stability of PSCs. In addition, lattice strain can be released by introducing pseudo-halides into perovskite. Cheng *et al*.[82] introduced a small amount of KBF_4 as an additive to elevate the quality of triple-cation mixed perovskite thin films. Substituting FA^+ with smaller A sites (MA^+ or Cs^+) may distort P-I-Pb bonds and thereby tilting the PbI_6 octahedron. One of the effective solutions is strain-compensation strategy by introducing smaller and larger ions together. In this case, the longer covalent bonds between BF_4^- and Pb^{2+}indicates larger effective radius and thus the introduction of BF_4^- can help balance the distorted lattice structure caused by the incorporation of smaller MA^+ and Cs^+, leading to released strain and decreased defect density.

Additive engineering

Additive engineering has emerged as a promising approach for regulating the strain of perovskite films without the need for incorporating into the perovskite lattice. Yalcinkaya *et al*.[64] employed a chemical method to regulate the strain in $MAPbI_3$ perovskite crystals by varying the ratio of $Pb(Ac)_2$ and $PbCl_2$ in the precursor solution. The effect on crystal strain was observed using a combination of PFM and XRD. The PFM images revealed an increased average size of ferroelastic twin domains with increasing $PbCl_2$ dosage, indicating an elevated level of crystal strain (Figure 8). This behavior arises due to a strain gradient during crystallization resulting from the different evaporation rates of methylammonium acetate and methylammonium chloride. Following precursor deposition, $MAPbI_3$ grains form closer to the surface while Cl-rich species remain at the bottom of the film. Upon annealing, MACl infiltrates the surface via ion exchange. This discrepancy leads to the formation of highly strained $MAPbI_3$ at room temperature in MA(Ac) areas, while I^-/Cl^- exchange occurs in Cl-rich areas, resulting in an increase in strain with increased $PbCl_2$ amount (Figure 15a). Zheng *et al*.[83] employed ammonium formate ($HCOONH_4$) as a preburied additive in the ETL to enable a bottom-up infiltration process for an in-situ and integral modification of the ETL, perovskite layer, and their interface. The $HCOONH_4$, which vaporizes during perovskite film annealing, facilitates high-quality perovskite grain growth due to the interaction between $HCOO^-$ and Pb^{2+} (Figure 15b). Ultimately, the $HCOONH_4$ treatment enhances electron extraction, releases residual strain of the perovskite film, and reduces defect densities within these layers. Min *et al*.[84] investigated the properties of $FAPbI_3$ perovskite films fabricated by adding trioctylphosphine (TOP) as a neutral ligand into the precursor solution. XRD analysis suggested that TOP relaxed the in-plane compressive strain by inducing a random orientation of the highly out-of-plane oriented $FAPbI_3$ film. The depth-dependent perovskite microstrain in the vertical direction was investigated by analyzing W-H plots obtained from XRD and GIWAXD. The application of a 0.28 mol% TOP-containing precursor solution to coat the resulted in the smallest strain. Additionally, to alleviate interfacial tensile strain, 2D Cl-terminated Ti_3C_2 ($Ti_3C_2Cl_x$) MXene[53] was introduced into the bulk and surface of $CsPbBr_3$ film. Arising from the strong interaction between Cl atoms in $Ti_3C_2Cl_x$ and under-coordinated Pb^{2+} in the $CsPbBr_3$ lattice, the expanded perovskite lattice was compressed and confined, in which the Pb-Cl bond played a role of "glue" and the 2D Ti_3C_2 immobilized the lattice (Figure 15c). Finally, the all-inorganic $CsPbBr_3$ PSC achieved an impressive champion efficiency of 11.08% with an ultrahigh V_{oc} reaching 1.702 V.

Zhang *et al*.[85] devised an innovative in-situ crosslinking-enabled strain-regulating crystallization (CSRC) method utilizing trimethylolpropane triacrylate (TMTA) to precisely regulate the top region of perovskite film, where the largest lattice distortion occurred (Figure 15d). TMTA, possessing mul-

DOI: 10.54227/elab.20230004

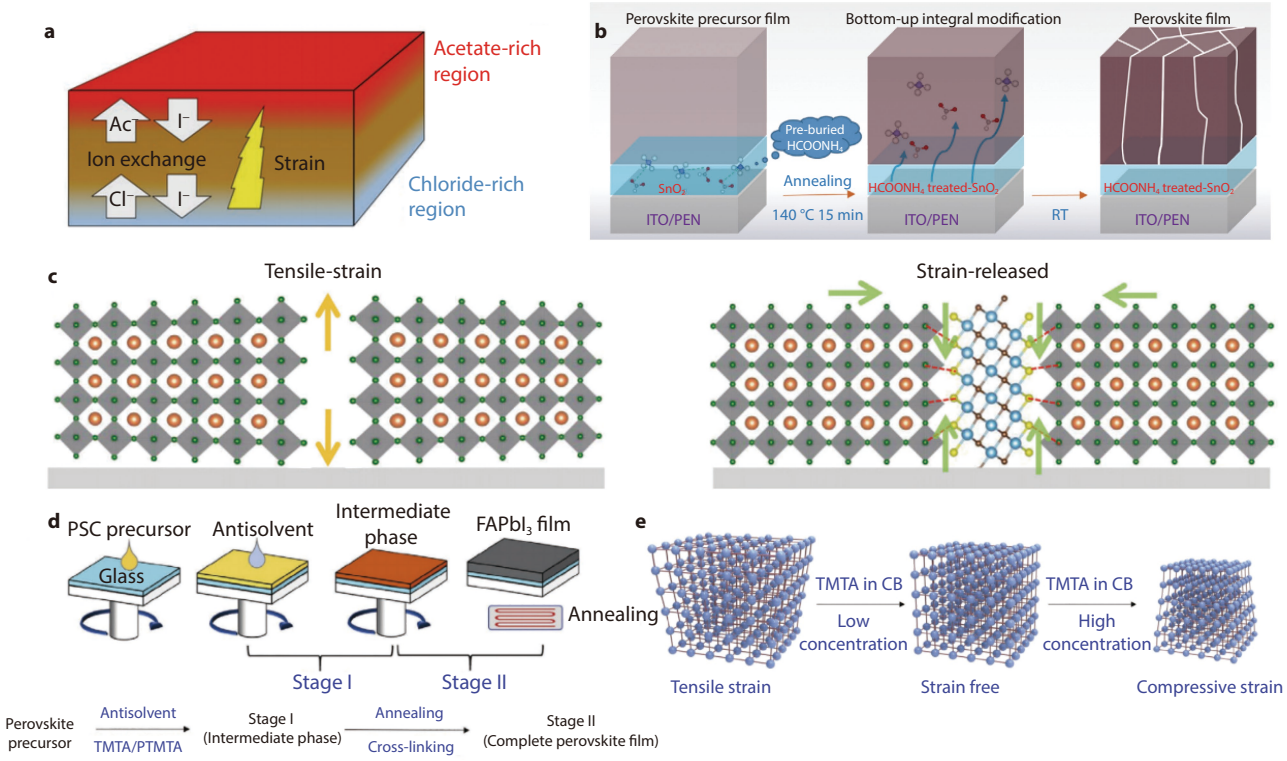

Fig. 15 **a** Illustration for strain mechanism.[64] Copyright 2022, Advanced Energy Materials. **b** Schematic illustration for the functionalization process of pre-buried $HCOONH_4$ additive.[83] Copyright 2022, Advanced Materials. **c** Schematic diagram for the residual strain in pristine $CsPbBr_3$ grains, schematic diagram of released strain in the reinforced $CsPbBr_3$ grains with Ti_3C_2Clx MXene.[53] Copyright 2021, Advanced Science. **d** The schematic representation for the tensile strain state of the control PSC film regulated by CSRC method. **e** Schematic illustration for the two stages of perovskite formation kinetic with TMTA-CSRC treatment.[85] Copyright 2021, Advanced Materials.

tiple functional groups of -OH and C=O, was introduced into antisolvent chlorobenzene to regulate the top region of the perovskite film during the crystallization process. During the perovskite crystal growth process, the perovskite nuclei bonded with TMTA molecules crosslinked with each other, forming compression confinement, which balanced the overall crystal thermal expansion. Molecule crosslinking pulled adjacent small perovskite grains together and facilitated their merging into larger perovskite grains. The perovskite film underwent a transition from tensile strain in the control film to strain-free and subsequently to compression strain, with increasing TMTA concentration. (Figure 15e). Hu *et al.*[86] proposed an imprint-assisted FAI compensation strategy to regulate residual lattice strain. The formation of perovskite crystalline at high temperature unavoidably results in a temperature gradient between the surface and bottom of the perovskite layer, leading to the detachment of FA^+ from the bottom and subsequent decomposition of perovskite crystals during the high-temperature annealing process. Due to the different cooling rates of the surface and core of the perovskite film, as well as the inhomogeneity of FA^+, non-uniform distortion may arise. To address this issue, an FAI film was stacked on top of the perovskite film and their surfaces were closely pressed together using a flap stamp. Subsequently, heat (180 °C) and pressure (0.6 MPa) were applied to two plates perpendicular to the joint surface to reinforce the interaction, enabling organic cations to diffuse from the top to bottom and achieve a high-quality perovskite film with uniform composition distribution. Finally the flap stamp was detached, and the residual lattice strain was effectively relieved along with further perovskite grain growth and coalescence, enhanced crystallinity, and repaired defects.

Heat treatment strategies

It is widely recognized that thermal expansion mismatch between the perovskite film and the substrate during thermal annealing is a significant source of strain in perovskite films. Therefore, heat treatment is considered one of the most straightforward methods to alleviate thermal strain during the fabrication process.

Modified annealing process

In a study by Huang *et al.*,[13] XRD measurements were conducted on $MAPbI_3$ thin films on ITO substrates at 100 °C, revealing no apparent strain in the films (Figure 16a). The evolution of XRD peak during cooling process from 100 °C to room temperature indicated gradual appearance of strain in the perovskite films. As thermal expansion of the lattice could account for the peak shift, the peak shift of the scraped $MAPbI_3$ powder was also measured over the same temperature range. However, the peak shift was found to be much smaller in the powder sample than that in the perovskite film (Figure 16b), indicating that the observed peak shift in the perovskite film was indeed due to the introduction of strain. To investigate further, the authors also prepared $MAPbI_3$ films at room temperature by drying the as-spun $MAPbI_3$·DMSO intermediate phase by evacuating for 3 days, rather than annealing at 100

DOI: 10.54227/elab.20230004

°C. The XRD patterns of the $MAPbI_3$ film, prepared at room temperature, were found to be consistent with those of unstrained perovskite crystals. Liu *et al.*[87] conducted an investigation on the potential correlation between strain and chemical gradients by driving the $CH_3NH_3PbI_3$ film away from its equilibrium state through heating, while simultaneously monitoring the evolution of strain and chemical gradient. The strain distribution within the $CH_3NH_3PbI_3$ film was analyzed using XRD and GIXRD. As the strain gradient decreased with heating to 45 °C and 70 °C, the distribution of $CH_3NH_3^+$ ion became more homogeneous throughout the depth of $CH_3NH_3PbI_3$ film.

Chen *et al.*[35] attempted to modulate the in-plane residual strain gradient in $(FAPbI_3)_{0.85}(MAPbBr_3)_{0.15}$ perovskite film by adjusting the annealing process. To achieve this , they used an inverted temperature gradient by flipping the thin film during heat treatment. The results were remarkable, with a significant reduction in tensile strain. The perovskite film showed a near-homogeneous lattice structure, with a small strain gradient and uniform lattice distance. Furthermore, they attempted to directly apply the inverted annealing process to the intermediate state after spin-coating, with the expectation of inducing a compressive strain with a vertical gradient across the film. Interestingly, the as-prepared films exhibited fitting curves with positive slopes that increased with the probe depth, indicating the presence of compressive strain in a vertical gradient. Zhao *et al.*[88] demonstrated precise strain control in monolayer aligned, large-grained $CsPbBr_3$ perovskite films to eliminate the strain-induced grain boundaries and pinhole-induced charge recombination. By carefully adjusting the $PbBr_2$ crystallization temperature, they pre-expanded the $PbBr_2$ films to create an abundance of holes, allowing for effective diffusion of the CsBr precursor and its conversion into $CsPbBr_3$ perovskite (Figure 16c). Arising from lattice-volume-expansion effect, sufficient space within the $PbBr_2$ matrix enabled the growth of $CsPbBr_3$ grains free of compressive strain, resulting in larger grain size and lower grain boundary densities. The best all-inorganic $CsPbBr_3$ PSC achieved a champion PCE as high as 10.71% and an ultrahigh voltage of 1.622 V.

Rolston *et al.*[39] implemented a modified anti-solvent technique in which MAI/PbI_2 films were spin-coated and then submerged in a diethyl ether (DEE) bath to convert the film to perovskite at room temperature (Figure 16d). They used a low boiling-point solvent to eliminate any residual anti-solvent. The perovskite phase was successfully obtained within 2 min of DEE bath, as evidenced by the darkending of the film. Subsequently, the films were subjected to thermal annealing at different temperatures (25 °C, 60 °C, or 100 °C). Notably, no significant change in the film morphology or color were ob-

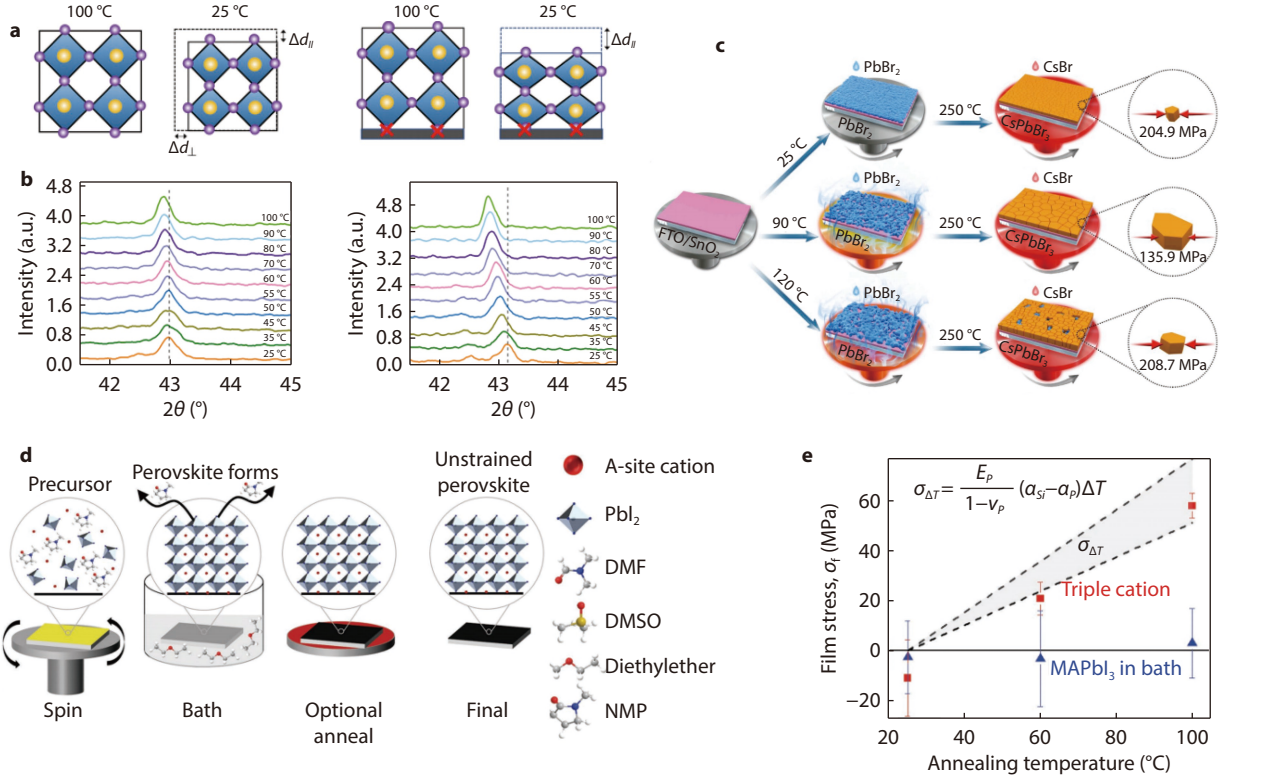

Fig. 16 **a** The perovskite forming at 100°C contracts vertically and laterally during cooling without and with substrate. **b** In-situ out-of-plane XRD patterns of scraped powders and annealed films at different temperatures.[13] Copyright 2017, Science Advances **c** Diagram of converting $PbBr_2$ into perovskites at low, intermediated and high temperatures as well as compression strains of perovskites.[88] Copyright 2020, Nano Energy. **d** Schematic illustration for the film formation during perovskite film formation and the effect on molecular structure for antisolvent processing of perovskite with using a bath conversion after spin-coating. **e** Measured stress for CsMAFA (red) formed at 25, 60 and 100 °C. Measured stress for $MAPbI_3$ (blue) formed at room temperature and with a post anneal at either 25, 60, or 100 °C, showing low stress values in all cases since the perovskite was fully converted before annealing.[39] Copyright 2022, Advanced Energy Materials.

DOI: 10.54227/elab.20230004

served during this annealing process, and measured strains remained unchanged (Figure 16e). Specifically, the residual strains for the films annealed at 100 °C, 60 °C and 25 °C were determined to be 3.0 ± 14.5 MPa, −3.2 ± 19.0 MPa, and −2.6 ± 14.5 MPa, respectively. These findings suggest that the residual strains in bath-converted perovskite films are not affected by further processing steps requiring elevated temperatures, such as the deposition of subsequent charge transport layers. However, it should be noted that the use of this technique at low temperature may result in lower quality perovskite film and consequently decreased device performance.[63]

One promising strategy to address thermal expansion mismatch between perovskite and substrates, commonly represented by indium tin oxide (ITO) or fluorine-doped tin oxide (FTO) glass substrate, is to use substrates with higher thermal expansion coefficients, such as polycarbonate (PC) or polyethylene terephthalate (PET).[15] Huang *et al*.[13] employed a flexible PET substrate with a thermal expansion coefficient of 2×10^{-5} ~ 8×10^{-5} K^{-1}, close to that of $MAPbI_3$, and found that the lattice strain in the $MAPbI_3$ film on the PET substrate was much lower than that upon ITO/glass substrate. Kim *et al*.[89] incorporated poly(4-butylphenyldiphenylamine) (pTPD), which has a higher thermal expansion coefficient than perovskite, between the perovskite layer and an adjacent layer to induce compressive strain in the perovskite film. The greater contraction of pTPD during the cooling process generated compressive strain in the perovskite film, which was confirmed by GIXRD characterization.

Heat treatment strategies

Xue *et al*.[15] developed a strain-compensation strategy to mitigate the thermal tensile strain in perovskite films by applying an external compressive strain produced by a top functional layer. The polymer hole transport layer (HTL) was critical to this strain compensation strategy, owing to its high thermal expansion coefficient, strong binding affinity for the perovskite layer, and high processing temperature. By adjusting the processing temperature of poly [5,5-bis(2-butyloctyl)-(2,2-bithiophene)-4,4′-dicarboxylate-alt-5,5′-2,2′-bithiophene] (PDCBT), perovskite films with adjustable strains, ranging from tensile to compressive, were produced. The introduced compressive strain can effectively offset the residual tensile strain when PDCBT was coated at high temperatures. Figure 17a depicts a linear correlation between stress and PDCBT coating temperature. Additionally, they discovered that compressive strain increased the intrinsic stability of perovskite halides by raising the activation energy for ion migration, thereby further improving the photostability and thermal stability of PSCs.

The instability of 2D/3D heterostructures has been attributed to the lattice expansion of strained 2D perovskite under common thermal processing conditions. However, an innovative fabrication technology has been reported by Mai *et al*.,[90] which involves the use of a compressively strained PEA_2PbI_4 layer to compensate for the internal tensile strain and stabilize the 2D/3D heterostructure. As depicted in Figure 17b, 3D perovskite films were fabricated through one-step spin-coating, followed by deposition of PEAI dissolved in isopropanol on top of 3D perovskite, and finally annealing process was carried out after covering the structure with PCBM. The tensile strain of the optimal sample was reduced to 983 MPa (Figure 17c-d). Due to the strong PCBM-iodide interaction in perovskite devices, PEAI will be well anchored by PCBM. The mismatch of thermal expansion coefficients between the two layers is utilized to realize strain compensation. As illustrated in Figure 17e, PEA_2PbI_4, which is anchored by PCBM with a low thermal expansion coefficient, experiences less stretching along the direction parallel to the substrate, resulting in the release of its tensile strain. Furthermore, the $[PbI_6]^{4-}$ octahedra in PEA_2PbI_4 embedded in the sandwich structure (3D perovskite/PEA_2PbI_4/PCBM) can hardly move due to clamping on both sides, implying that MA^+ and I^+ ions are less likely to migrate into the 2D perovskite. The peak positions of 2D perovskite films show only a slight shift even after 253 h of thermal annealing when the films are covered by PCBM (Figure 17f).

Interfacial management

ETL/perovskite interface

To alleviate the interface strain between SnO_2 ETL and perovskite layer, Meng *et al*.[91] introduced polystyrene (PS) as a buffer layer on top of the SnO_2 layer. By utilizing the soft, glassy state of PS at 150 °C, which is much lower than the annealing temperature of perovskite, they were able to avoid the substrate limit during the growth process of perovskite grains. As a result, the perovskite with a strain-released lattice was obtained (Figure 18a). Zhou *et al*.[92] demonstrated interfacial strain relaxation by introducing a 2D WS_2 nanoflake at the SnO_2-TiO_xCl_{4-2x}/$CsPbBr_3$ interface. A high-quality $CsPbBr_3$ perovskite film was grown on the WS_2 nanoflakes according to van der Waals epitaxy due to the matched lattices. During the annealing and cooling processes, the weak interaction between WS_2 and perovskite acted as a "lubricant" to release the interfacial tensile strain (Figure 18b). The resulting strain-released device with WS_2/$CsPbBr_3$ van der Waals heterostructure achieved an enhanced efficiency from 9.27% to 10.65%, with an ultrahigh V_{oc} of 1.70 V. Similarly, Bi *et al*.[93] developed a multifunctional interface modification strategy by incorporating potassium hexafluorophosphate (KPF_6) to modify SnO_2/perovskite interface. KPF_6 serve as a "lubricant" between ETL and perovskite to release residual strain. Wu *et al*.[49] introduced MXene to modify the electronic property of SnO_2 and passivate the interface between the perovskite and the SnO_2. The lattice matching of MXene and perovskite induced vertically aligned crystal growth of perovskites by suppressing the generation of concentrated strain during perovskite growth.

Zhang *et al*.[94] introduced different Li salts (Li_2CO_3, $Li_2C_2O_4$ and $CHLiO_2$) into SnO_2-based $FAPbI_3$ PSCs as the multifunctional layers at the ETL/perovskite interface to investigate the effect of molecular configuration on the adjacent layer. CO_3^{2-} shown stronger hydrogen bonding with FA^+ due to its more negative adsorption energy value of −4.78 eV, compared to −3.99 and −4.56 eV for $C_2O_4^{2-}$ and $HCOO^-$, respectively. In addition, the authors demonstrated that these anions could passivate the FA^+ defects, as evidenced by the increase in formation energy of FA^+ vacancies from 3.80 to 4.91, 4.20, and 4.80 eV upon the adsorption of CO_3^{2-}, $C_2O_4^{2-}$ and $HCOO^-$, respectively. The results indicated that CO_3^{2-} can passivate the FA^+ defect more effectively than the other two anions. Moreover,

DOI: 10.54227/elab.20230004

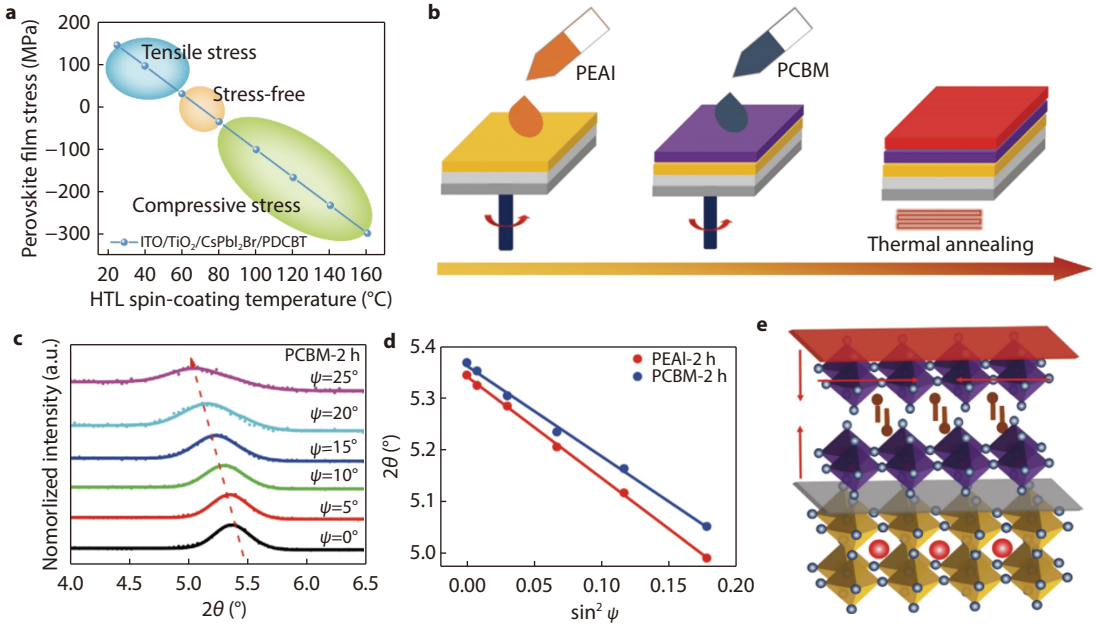

Fig. 17 **a** The calculated net average stress in perovskites within the structures consisting of ITO/TiO_2/perovskite/PDCBT as a function of PDCBT spin-coating temperature.[15] Copyright 2020. Nature Communications. **b** Optimized 2D/3D perovskite processing procedures. **c** GIXRD spectra at different tilt angles for the PCBM-2 h thin film. **d** Residual tensile strains of PEA_2PbI_4 films under different preparation technologies. **e** Schematic diagram for strain compensation caused by covering PCBM. **f** Magnified diffraction peaks of (002) plane from 2D perovskite.[90] Copyright 2020, Advanced Energy Materials.

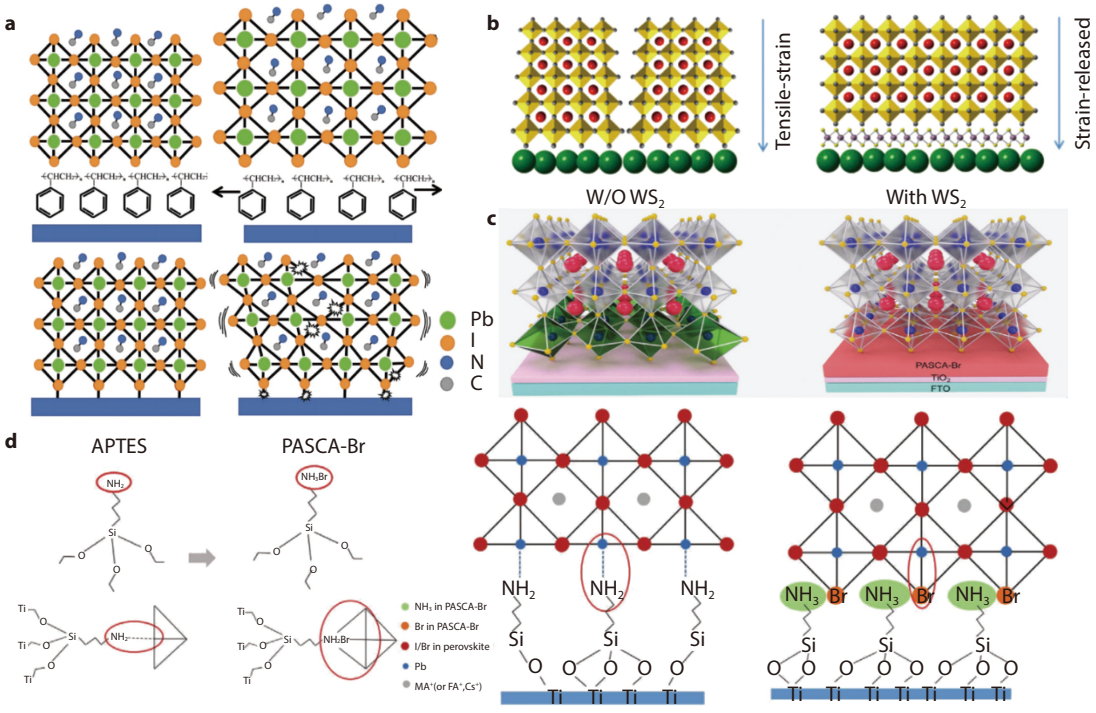

Fig. 18 **a** Schematic illustration for the PS buffer layer to release the strain: as-prepared perovskite films with PS, annealed perovskite films with PS, as-prepared perovskite films without PS, and annealed perovskite films without PS.[91] Copyright 2019, Advanced Functional Materials. **b** Schematic diagram for the residual strain distribution in $CsPbBr_3$ grains with and without WS_2 interlayer.[92] Copyright 2020, Angewandte Chemie International Edition. **c** A schematic of perovskite crystals at the interface. **d** Protonated amino terminals (R-NH_3Br) and lattice structure of APTES and PASCA-Br modified interfaces.[93] Copyright 2020, Advanced Materials.

the Sn *3d* peaks exhibited the largest shift in the Li_2CO_3-modified film, implying stronger interaction with SnO_2 than the other two. Thus, the triangle configuration of C=O and two C–O (CO_3^{2-}) produced the strongest interaction with the ad-

DOI: 10.54227/elab.20230004

jacent layer and resulted in the lowest defect density. Typically, larger residual strain is associated with more defects due to the perovskite lattice distortion. As a result, XRD and GIXRD results suggest that Li_2CO_3 can most effectively mitigate the internal strain in the $FAPbI_3$ films. Zhang *et al*.[95] introduced a protonated amine silane coupling agent (PASCA-Br) between TiO_2 and perovskite layers. PASCA-Br simultaneously held TiO_2 and perovskite crystals and served as the ideal growth substrate for perovskite. This strategy released the strain at the TiO_2/perovskite interface by perovskite lattice distortion, as shown in Figure 18c. The protonated alkyl ammonium bromide terminals ($R\text{-}NH_3Br$) targeted bare under-coordinated Pb atoms and compensated for mutilated octahedrons on the surfaces. That means NH_3^+ could partially act as an A-site for newly formed perovskite crystals (Figure 18d). Similarly, Liu *et al*.[96] introduced alkyltrimethoxysilane strain-release layers (SRLs) at the perovskite/ETL interface to mitigate lattice distortion and alleviate strain. They determined that the SRL with the longest alkyl chain was the most effective at reducing interfacial lattice distortion, resulting in improved charge transfer at the perovskite/ETL interface and enhanced phase/device stability. The authors inferred that SRLs with longer alkyl chains provide a more flexible interface, thereby improving their ability to decrease the thermal expansion mismatch between the perovskite and ETL, ultimately leading to a less strained interface.

Lv *et al*.[97] proposed a dynamic strategy for controlling perovskite film formation through the creation of a soft perovskite-substrate interface composed of amphiphilic soft molecules (ASMs) featuring long alkyl chains and Lewis base groups. The hydrophobic alkyl chains of the ASMs interacted with poly(triarylamine) (PTAA) greatly improved the wettability of PTAA, promoting the nucleation and growth of perovskite crystals, while the Lewis base groups that bound to perovskite lattices significantly passivated the defects. Of particular note, the soft perovskite-substrate interface with ASMs dynamically matched the lattice distortion with reduced interfacial residual strain during perovskite crystallization thanks to the soft self-adaptive nature of the long-chains.

Perovskite/HTL interface

Chen *et al*.[50] stabilized FA-based perovskite through toughening the interface with a symmetric molecule of 1,1′-(Methylenedi-4,1-phenylene) bismaleimide (BMI). GIXRD characterization revealed that the BMI modification effectively regulated the strain at the surface for compressively-strained films, with a value of approximately 7.4 MPa (Figure 19a). The authors investigate the strain state in the depth of 500 nm from the surface of the perovskite film and found that the BMI modification-induced compressed strain could be transferred from the surface to the bulk of perovskite films, with a slightly compressed strain observed. Figure 19b illustrates a Pb-I frame plane perpendicular to the *b*-axis, where two Pb atoms bind with the BMI. The layers 1, 2 and 3 are fixed boundary conditions, and other layers have complete degrees of freedom. The values of $d_{3,4}$ and $d_{4,5}$ are 6.26 Å and 6.35 Å, respectively, both of which are shorter than the pristine unit cell lattice data *a* (6.41 Å), indicating a compressed strain along the *a*-axis. Meanwhile, the BMI bears tension strain from perovskite, as evidenced by the elongation of the distance between the O atoms of BMI and Pb to 10.70 Å, compared with the initial value of 10.63 Å. These findings are consistent with the GIXRD results, indicating that the BMI-modified perovskite film bears biaxial in-plane compressive strain. Zheng *et al*.[98] proposed the utilization of the organic polymer J71 with N- and S-atoms to release internal strain in $CsPbI_2Br$ film (Figure 19c). Due to the thermal expansion mismatch between $CsPbI_2Br$ perovskite and ITO/SnO_2 substrate, a high temperature thermal annealing process generate a large residual strain in $CsPbI_2Br$ film, causing further lattice expansion and increasing the spacing between crystal planes. By modifying with J71, the N and S elements in J71 molecules bonded with Pb species in perovskite, producing force interactions that effectively offset the tensile strain in the crystal and shorten the crystal plane spacing (Figure 19d). The coordination between J71 and perovskite regulated the strain from tensile to compressive, among which the strain-free film could be realized at an optimal J71 concentration.

Yang *et al*.[99] incorporated an in-situ cross-linking polymerizable propargylammonium (PA^+) into the 3D perovskite film surfaces and grain boundaries to form a 1D/3D perovskite heterostructure. The PA^+ organic cations entered the grain boundary and interacting with each other by cross-linking to generate compression strain on perovskite thin films, thus allowing for the effective release of the residual tensile strain. Suo *et al*.[100] utilized cyclohexylmethylammoniumiodide (CMAI) as a passivation agent, along with either isopropanol (IPA) or chloroform (CF) as a carrier mediator into $FAPbI_3$. As formamidinium iodide (FAI) has a good solubility in IPA, exposure to IPA caused partial dissolution of FAI from the perovskite surface. During the spin-coating process, the dissolved FAI was removed, leaving vacancies for a reaction to occur between the remaining PbI_2 and the newly introduced CMAI. This reaction resulted in the formation of a 2D perovskite layer, as shown in Figure 19e. Conversely, when exposed to CF, CMAI had limited possibility to react with PbI_2 due to the insolubility of FAI in CF, thus resulting in an additional CMAI layer forming on top of the perovskite film. The distinct surface reconstruction processes by CMAI (IPA) and CMAI (CF) led to diverse surface composition, influencing the residual strain of the perovskite surface and the formation of the intrinsic strain. These effects, in turn, created a strain-free environment on the perovskite surface, leading to an improved efficiency of up to 24%.

External strain regulation

External mechanical force

In order to investigate the impacts of strain on film stability under illumination, Huang *et al*.[13] tuned the strain in the perovskite films by preparing a $MAPbI_3$ film on bendable glass substrate. To prevent the moisture-induced surface decomposition, a thin layer (40 nm in thickness) of PS was coated on top of the $MAPbI_3$ layer, and the film was then bent to a convex shape to increase the lattice strain or a concave shape to reduce the residual strain in the films (Figure 17e). The change in lattice strain was confirmed by out-of-plane XRD patterns, which shown that the lattice strains in the convex, flat and concave films were 0.62%, 0.47% and 0.2%, respectively. The three samples with different bending states were sealed together in a petri dish and illuminated with white

DOI: 10.54227/elab.20230004

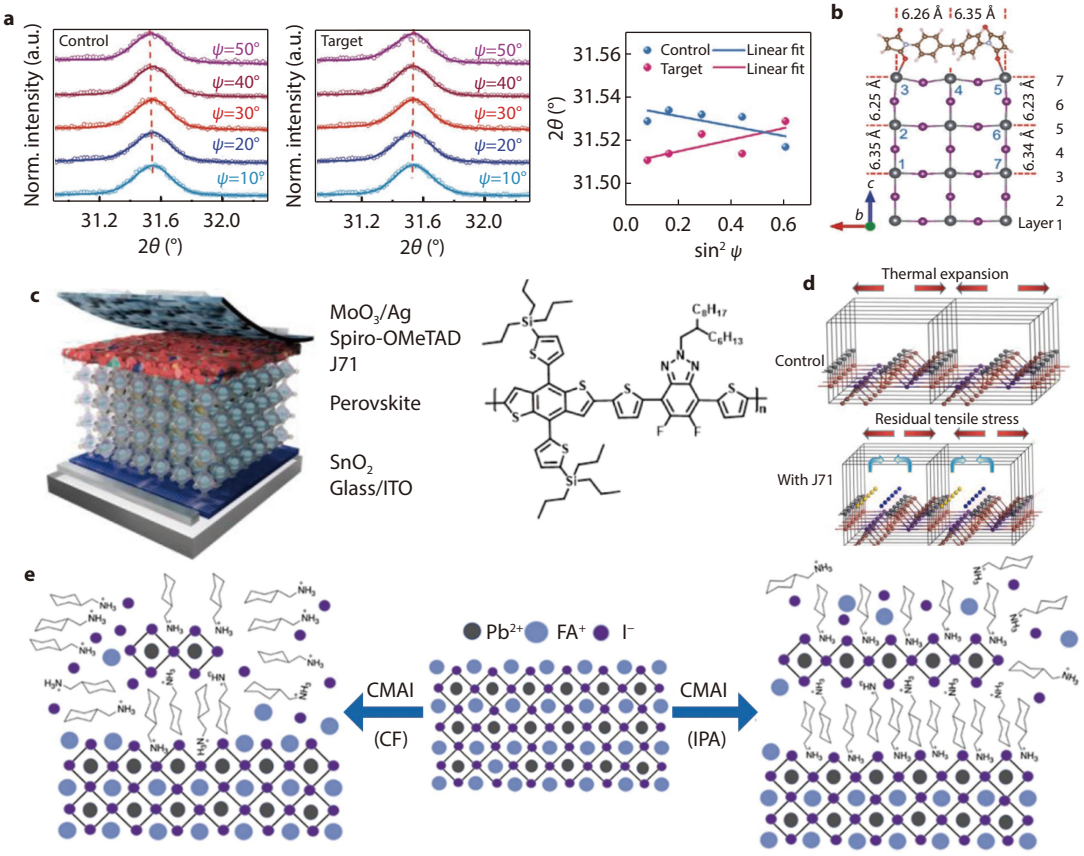

Fig. 19 **a** GIXRD spectra of control and target perovskite films with different instrumental tilt angles ψ values in the depth of 200 nm. Macroscope residual strain distribution analysis by linear fitting of 2θ-sin$^2\phi$ for control and target perovskite films. **b** Microstructure of Pb-I frame plane perpendicular to the b-axis, where two Pb atoms bind with the BMI.[50] Copyright 2022, Advanced Functional Materials. **c** Illustration of as-prepared $CsPbI_2Br$ solar cells with the structure of ITO/SnO_2/perovskite/J71/spiro-OMeTAD/MoO_3/Ag, molecular formula of J71 **d**, Crystal mechanics model of control and $CsPbI_2Br$/J71.[98] Copyright 2022, Chemical Engineering Journal. **e** Schematic representation of surface reconstruction process after CMAI (IPA) and CMAI (CF) treatment.[100] Copyright 2022, Nano Energy.

light at an intensity of 50 mW cm^{-2} for 500 h. After illumination, the bending force was removed, and the films were returned to the flat state for measurements. Photographs revealed that the films with larger lattice strain exhibited larger yellow areas (Figure 17e) due to the decomposition of $MAPbI_3$ into PbI_2. In contrast, the films with smaller strain remained mostly black after 500 h of illumination. These results were confirmed by the XRD pattern (Figure 17f). Wang *et al.*[101] designed a set of molds to bend the $MAPbI_3$ film with different bending radii. Due to the large thickness difference between the perovskite film (300 nm) and the PET substrate (175 μm), the strain applied on the substrate after bending was completely transferred to the $MAPbI_3$ film. As the convex bending curvature increased, the residual compressive strain was firstly released and then changed to tensile strain (Figure 20a). The charge carrier lifetime increased with increasing tensile strain, whereas it decreased with increasing compressive strain, as determined by TRPL analysis, which was further confirmed by transient absorption spectroscopy results. Luo *et al.*[102] reported a pressure-assisted solution processing (PASP) technique that enables the controllable fabrication of highly crystallized perovskite films with micron-sized grains by controlling perovskite nucleation and growth. The process involved spin-coating a precursor solution of triple cation perovskite onto a mesoporous TiO_2 film, followed by face-to-face combination of two perovskite films with varying pressures applied to the top film. After annealing at 110 °C for 60 min, the top film transformed into a smooth and highly crystalline bottom perovskite film (Figure 20b). Top-view SEM revealed a clear correlation between the pressure and the grain morphology of PASP-based perovskite films, with grain sizes gradually increasing (from few hundred nanometers to ~3 μm) by increasing the pressure from 1225 to 12250 Pa. However, the application of higher pressures, specifically between 7350 and 12250 Pa, resulted in the appearance of various cracks across the grain boundaries. While high crystallinity and large grain sizes are favorable for the photovoltaic performance of solar cells, cracks are detrimental. Therefore, PSCs with PASP-perovskite films achieved the highest PCE of 20.74% (stabilized efficiency of 20.33%) and exceptional stability against moisture and continuous light illumination with a pressure of 4900 Pa. Their findings provide a methodological foundation for enhancing the efficiency and durability of PSCs by controlloing crystal nucleation and growth to achieve enlarged grain sizes and reduced defects.

Illumination force

Tsai *et al.*[41] conducted a study where they exposed a stabilized mixed-cation pure-iodide perovskite film to continu-

DOI: 10.54227/elab.20230004

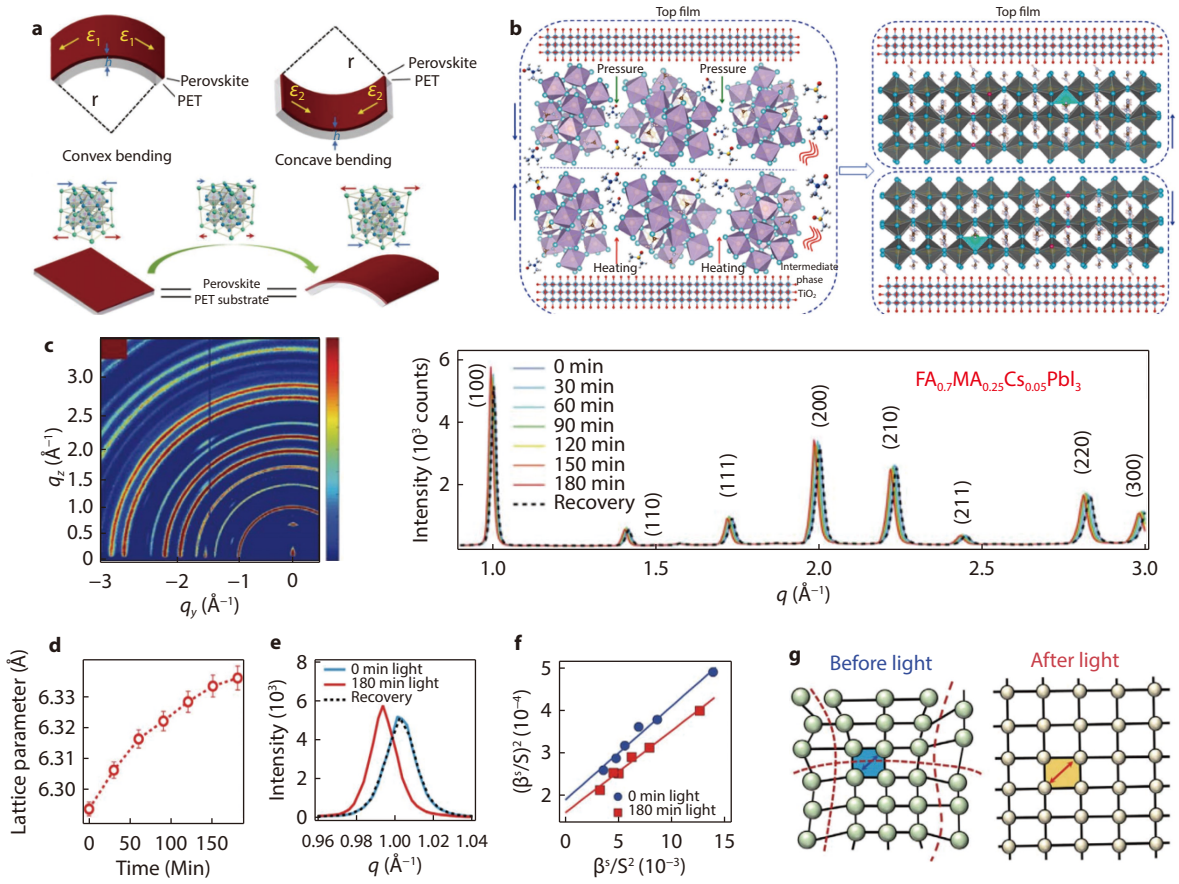

Fig. 20 **a** Schematic diagrams for convex, concave bending and lattice strain changes during a convex bending process.[101] Copyright 2020, Journal of Materials Chemistry C. **b** Schematic diagrams for convex, concave bending and lattice strain changes during a convex bending process.[102] Copyright 2020, Nano Energy. Light-induced lattice expansion and structural analyses. **c** A typical synchrotron diffraction pattern (left) and the line cut of GIWAXS maps (right) for $FA_{0.7}MA_{0.25}Cs_{0.05}PbI_3$ (cubic phase) thin films under various illumination times and the recovery spectra obtained after the films were kept in the dark for 30 min. q_y, vector along in-plane direction, and q_z, vector along out-of-plane direction in reciprocal space with respect to the substrate. **d** Lattice constant as a function of illumination time. **e** Peak change before and after 180 min of illumination and recovery in the dark. **f** Linear fit of integral-breadth analysis using Halder-Wagner plots, where *b* is the integral breadth of the diffraction peak and *S* is defined as $S = q/2p$. **g** Schematic illustration for the crystal structure change before (local distortion) and after illumination (lattice expansion).[41] Copyright 2018, Science.

ous light soaking by standard one sun illumination, resulting in a large and uniform lattice expansion (Figure 20g). The light induced lattice expansion increased the average structural correlation length and relaxed the local strain in the film. However, on phase segregation or degradation was observed, as shown by the absence of new Bragg peaks or splitting in the GIWAXS analysis after 180 min of continuous illumination. However, all of the diffraction peaks uniformly shifted toward lower values of scattering vector *q*, corresponding to an isotropic increase in lattice constant *d* (lattice expansion) from 6.290 ± 0.002 Å to 6.330 ± 0.004 Å (Figure 20c-d). Interestingly, the lattice expansion persisted for 30 min even after the film was removed from the light source, before relaxing back to its original value (Figure 20c, e). The illumination also enhanced crystallinity, as indicated by the increase in main-peak intensities and sharpening of peak widths after illumination (Figure 20e). The researchers further analyzed the crystallite size and strain distribution using a line profile analysis and found a decrease in microstrains and an increase in average crystallite size after light soaking (Figure 20f), suggesting relaxation of the local strain in hybrid perovskites containing multiple cations. A possible microscopic explanation for the lattice expansion (Figure 20g) was put forward by the authors, positing that the as-prepared thin film experiences strain due to the distorted lattice, which balances cations of different sizes. Upon exposure to illumination, the thin film undergoes volumetric expansion in all directions, thereby relaxing the local strain. This process reduces the mosaicity of the crystallites and sharpens the Bragg peaks.

Conclusions and Perspective

In summary, impressive progress has been made in pushing the state-of-the-art PCEs of PSCs to around 80% of the Shockley-Queisser limits. However, the residual strain in perovskite films remains a major hindrance to further enhancing PCEs. Thus, releasing the strain is a critical and cutting-edge topic in this field. This review underscores the significance of strain regulation in PSCs as a promising route for improving their optoelectronic properties and device stability. Herein, we outline the definition, origin, effects, and the regulation

DOI: 10.54227/elab.20230004

methods of residual strain in perovskites that impact the efficiency and stability of PSCs. Strain in perovskites can arise from internal and external factors. The internal strain in perovskite films includes local lattice strain due to $[BX_6]^{4-}$ octahedral tilts and distortion of crystal symmetry, as well as local lattice mismatch due to heterogeneous crystallization. The external condition-induced strain includes the strain of perovskite layer caused by lattice and thermal expansion mismatch and external strain conditions, such as light, temperature, electrical bias, and external pressure. Characterization methods for strain in perovskite films are systematically categorized as XRD, GIWAXS, Raman spectroscopy, TEM, SED, EBSD, and PFM. The impacts of strain on perovskite films and device performance, including band structure, defect properties, ion migration, phase and device stability, is complex. Finally, this review summarizes the previous strain regulation strategies of perovskite films, which can be divided into compositional engineering, heat treatment strategies, interface management, and external strain regulation methods.

Despite extensive studies on the formation and regulation of strains in halide perovskites, there is still a lack of precise and effective strain regulation strategies, and the evolution and distribution of strain on nanoscale need to be uncovered. Lattice mismatch-induced strain can be alleviated by doping foreign ions, but the type and concentration of dopants can affect the physical properties of the material, which may reduce the device efficiency and stability. Although low-temperature fabrication of perovskite films can reduce tensile strain in perovskite film, it can also reduce the device performance. In order to commercialize PSCs, large-area and flexible devices are necessary, but the effectiveness of strategies to release strain in perovskite layers in these devices remains to be discussed. Several strain regulation strategies can potentially enhance the stability and performance of PSCs. Firstly, developing novel substrates with comparable thermal expansion coefficients to perovskites and enabling the formation of high-quality perovskite films deposited upon them is critical for achieving excellent optoelectronic properties of PSCs. Secondly, exploring more effective strategies to simultaneously passivate defects and release residual strain, such as in-situ crosslinking, can enhance the performance of PSCs. Thirdly, investigating novel fabrication methods for perovskite films under low temperature can reduce residual strain caused by thermal expansion mismatch. Fourthly, developing new additives and interfacial materials to suture grain boundaries and interfaces between perovskite/ETL (or HTL), where local strain concentration usually occurs, can further enhance PSC performance. Finally, exploring in-situ strain compensation strategies is critical in the construction of perovskite/perovskite and perovskite/silicon tandems, where many layers could form strains that affect overall efficiency and stability.

CONFLICT OF INTEREST

The authors declare no conflict of interest.

AUTHOR CONTRIBUTIONS

Q. Tang directed the overall process. Y. Zhao and Q. Tang conceived the framework of the review. Y. Zhao, Q. Wang, Y. Teng, Z. Xin, and Y. Cao researched data and wrote the first draft. Q. Tang, Y. Zhao, and Q. Wang revised the manuscript.

REFERENCES

1. W. Zhang, Y. Chao, S. Guo, *Energy Lab*, 2023, 1, 220004
2. S. Liu, S. Yin, L. Cui, H. Yu, K. Deng, Z. Wang, Y. Xu, L. Wang, H. Wang, *Energy Lab*, 2023, 1, 220005
3. G. E. Eperon, S. D. Stranks, C. Menelaou, M. B. Johnston, L. M. Herz, H. J. Snaith, *Energy & Environmental Science*, 2014, 7, 982
4. S. De Wolf, J. Holovsky, S. J. Moon, P. Loper, B. Niesen, M. Ledinsky, F. J. Haug, J. H. Yum, C. Ballif, *The Journal of Physical Chemistry Letters*, 2014, 5, 1035
5. L. M. Herz, *ACS Energy Letters*, 2017, 2, 1539
6. S. D. Stranks, G. E. Eperon, G. Grancini, C. Menelaou, M. J. Alcocer, T. Leijtens, L. M. Herz, A. Petrozza, H. J. Snaith, *Science*, 2013, 342, 341
7. https://www.nrel.gov/pv/interactive-cell-efficiency.html (accessed: October, 2023)
8. M. I. Saidaminov, J. Kim, A. Jain, R. Quintero-Bermudez, H. Tan, G. Long, F. Tan, A. Johnston, Y. Zhao, O. Voznyy, E. H. Sargent, *Nature Energy*, 2018, 3, 648
9. J. Wu, S. C. Liu, Z. Li, S. Wang, D. J. Xue, Y. Lin, J. S. Hu, *National Science Review*, 2021, 8, nwab047
10. T. W. Jones, A. Osherov, M. Alsari, M. Sponseller, B. C. Duck, Y.-K. Jung, C. Settens, F. Niroui, R. Brenes, C. V. Stan, Y. Li, M. Abdi-Jalebi, N. Tamura, J. E. Macdonald, M. Burghammer, R. H. Friend, V. Bulović, A. Walsh, G. J. Wilson, S. Lilliu, S. D. Stranks, *Energy & Environmental Science*, 2019, 12, 596
11. M. V. Khenkin, E. A. Katz, A. Abate, G. Bardizza, J. J. Berry, C. Brabec, F. Brunetti, V. Bulović, Q. Burlingame, A. Di Carlo, R. Cheacharoen, Y.-B. Cheng, A. Colsmann, S. Cros, K. Domanski, M. Dusza, C. J. Fell, S. R. Forrest, Y. Galagan, D. Di Girolamo, M. Grätzel, A. Hagfeldt, E. von Hauff, H. Hoppe, J. Kettle, H. Köbler, M. S. Leite, S. Liu, Y.-L. Loo, J. M. Luther, C.-Q. Ma, M. Madsen, M. Manceau, M. Matheron, M. McGehee, R. Meitzner, M. K. Nazeeruddin, A. F. Nogueira, Ç. Odabaşı, A. Osherov, N.-G. Park, M. O. Reese, F. De Rossi, M. Saliba, U. S. Schubert, H. J. Snaith, S. D. Stranks, W. Tress, P. A. Troshin, V. Turkovic, S. Veenstra, I. Visoly-Fisher, A. Walsh, T. Watson, H. Xie, R. Yıldırım, S. M. Zakeeruddin, K. Zhu, M. Lira-Cantu, *Nature Energy*, 2020, 5, 35
12. J. A. Steele, H. Jin, I. Dovgaliuk, R. F. Berger, T. Braeckevelt, H. Yuan, C. Martin, E. Solano, K. Lejaeghere, S. M. J. Rogge, C. Notebaert, W. Vandezande, K. P. F. Janssen, B. Goderis, E. Debroye, Y.-K. Wang, Y. Dong, D. Ma, M. Saidaminov, H. Tan, Z. Lu, V. Dyadkin, D. Chernyshov, V. Van Speybroeck, E. H. Sargent, J. Hofkens, M. B. J. Roeffaers, *Science*, 2019, 365, 679
13. J. Zhao, Y. Deng, H. Wei, X. Zheng, Z. Yu, Y. Shao, J. E. Shield, J. Huang, *Science Advances*, 2017, 3, eaao5616
14. N. N. Som, P. M. W. P. Sampath, S. D. Dabhi, V. Mankad, S. Shinde, M. L. C. Attygalle, P. K. Jha, *Solar Energy*, 2018, 173, 1315
15. D. J. Xue, Y. Hou, S. C. Liu, M. Wei, B. Chen, Z. Huang, Z. Li, B. Sun, A. H. Proppe, Y. Dong, M. I. Saidaminov, S. O. Kelley, J. S. Hu, E. H. Sargent, *Nature Communications*, 2020, 11, 1514
16. Y. Chen, Y. Lei, Y. Li, Y. Yu, J. Cai, M. H. Chiu, R. Rao, Y. Gu, C. Wang, W. Choi, H. Hu, C. Wang, Y. Li, J. Song, J. Zhang, B. Qi, M. Lin, Z. Zhang, A. E. Islam, B. Maruyama, S. Dayeh, L. J. Li, K. Yang, Y. H. Lo, S. Xu, *Nature*, 2020, 577, 209
17. G. Liu, L. Kong, J. Gong, W. Yang, H. k. Mao, Q. Hu, Z. Liu, R. D. Schaller, D. Zhang, T. Xu, *Advanced Functional Materials*, 2016, 27, 1604208
18. S. Jiang, Y. Fang, R. Li, H. Xiao, J. Crowley, C. Wang, T. J. White, W. A. Goddard, 3rd, Z. Wang, T. Baikie, J. Fang, *Angewandte Chemie International Edition*, 2016, 55, 6540

DOI: 10.54227/elab.20230004

19. H. Yu, Q. Sun, T. Zhang, X. Zhang, Y. Shen, M. Wang, *Materials Today Energy*, 2021, 19, 100601
20. J. H. Im, C. R. Lee, J. W. Lee, S. W. Park, N. G. Park, *Nanoscale*, 2011, 3, 4088
21. Y. Fu, H. Zhu, Chen. J, M. P. Hautzinger, X. Zhu, S. J, *Nature Reviews Materials*, 2019, 4, 169
22. Y. Jiao, S. Yi, H. Wang, B. Li, W. Hao, L. Pan, Y. Shi, X. Li, P. Liu, H. Zhang, C. Gao, J. Zhao, J. Lu, *Advanced Functional Materials*, 2020, 31, 2006243
23. Y. Dang, Y. Liu, Y. Sun, D. Yuan, X. Liu, W. Lu, G. Liu, H. Xia, X. Tao, *CrystEngComm*, 2015, 17, 665
24. N. K. McKinnon, D. C. Reeves, M. H. Akabas, *Journal of General Physiology*, 2011, 138, 453
25. G. Kim, H. Min, K. S. Lee, D. Y. Lee, S. M. Yoon, S. I. Seok, *Science*, 2020, 370, 108
26. X. Zheng, C. Wu, S. K. Jha, Z. Li, K. Zhu, S. Priya, *ACS Energy Letters*, 2016, 1, 1014
27. W. Travis, E. N. K. Glover, H. Bronstein, D. O. Scanlon, R. G. Palgrave, *Chemical Science*, 2016, 7, 4548
28. D. Liu, W. Zha, Y. Guo, R. Sa, *ACS Omega*, 2020, 5, 893
29. J.-H. Lee, N. C. Bristowe, J. H. Lee, S.-H. Lee, P. D. Bristowe, A. K. Cheetham, H. M. Jang, *Chemistry of Materials*, 2016, 28, 4259
30. L.-J. Ji, S.-J. Sun, Y. Qin, K. Li, W. Li, *Coordination Chemistry Reviews*, 2019, 391, 15
31. Q. A. Akkerman, L. Manna, *ACS Energy Letters*, 2020, 5, 604
32. R. J. Sutton, M. R. Filip, A. A. Haghighirad, N. Sakai, B. Wenger, F. Giustino, H. J. Snaith, *ACS Energy Letters*, 2018, 3, 1787
33. B. Wang, N. Novendra, A. Navrotsky, *Journal of the American Chemical Society*, 2019, 141, 14501
34. F. Bertolotti, L. Protesescu, M. V. Kovalenko, S. Yakunin, A. Cervellino, S. J. L. Billinge, M. W. Terban, J. S. Pedersen, N. Masciocchi, A. Guagliardi, *ACS Nano*, 2017, 11, 3819
35. C. Zhu, X. Niu, Y. Fu, N. Li, C. Hu, Y. Chen, X. He, G. Na, P. Liu, H. Zai, Y. Ge, Y. Lu, X. Ke, Y. Bai, S. Yang, P. Chen, Y. Li, M. Sui, L. Zhang, H. Zhou, Q. Chen, *Nature Communications*, 2019, 10, 815
36. I. Mela, C. Poudel, M. Anaya, G. Delport, K. Frohna, S. Macpherson, T. A. S. Doherty, A. Scheeder, S. D. Stranks, C. F. Kaminski, *Advanced Functional Materials*, 2021, 31, 2100293
37. S. Jariwala, H. Sun, G. W. P. Adhyaksa, A. Lof, L. A. Muscarella, B. Ehrler, E. C. Garnett, D. S. Ginger, *Joule*, 2019, 3, 3048
38. D. Liu, D. Luo, A. N. Iqbal, K. W. P. Orr, T. A. S. Doherty, Z. H. Lu, S. D. Stranks, W. Zhang, *Nature Materials*, 2021, 20, 1337
39. N. Rolston, K. A. Bush, A. D. Printz, A. Gold-Parker, Y. Ding, M. F. Toney, M. D. McGehee, R. H. Dauskardt, *Advanced Energy Materials*, 2018, 8, 1802139
40. L. A. Muscarella, E. M. Hutter, F. Wittmann, Y. W. Woo, Y. K. Jung, L. McGovern, J. Versluis, A. Walsh, H. J. Bakker, B. Ehrler, *ACS Energy Letters*, 2020, 5, 3152
41. H. Tsai, R. Asadpour, J.-C. Blancon, C. C. Stoumpos, O. Durand, J. W. Strzalka, B. Chen, R. Verduzco, P. M. Ajayan, S. Tretiak, J. Even, M. A. Alam, M. G. Kanatzidis, W. Nie, A. D. Mohite, *Science*, 2018, 360, 67
42. D. Kim, J. S. Yun, P. Sharma, D. S. Lee, J. Kim, A. M. Soufiani, S. Huang, M. A. Green, A. W. Y. Ho-Baillie, J. Seidel, *Nature Communications*, 2019, 10, 444
43. E. Strelcov, Q. Dong, T. Li, J. Chae, Y. Shao, Y. Deng, A. Gruverman, J. Huang, A. Centrone, *Science Advances*, 2017, 3, 1602165
44. Y. Liu, B. G. Sumpter, J. K. Keum, B. Hu, M. Ahmadi, O. S. Ovchinnikova, *ACS Applied Energy Materials*, 2021, 4, 2068
45. A. Khorsand Zak, W. H. Abd. Majid, M. E. Abrishami, R. Yousefi, *Solid State Sciences*, 2011, 13, 251
46. C. Wang, C. Zuo, Q. Chen, L. Ding, *Journal of Semiconductors*, 2021, 42, 060201
47. M. Qin, P. F. Chan, X. Lu, *Advanced Materials*, 2021, 33, 2105290
48. W. Hui, Y. Xu, F. Xia, H. Lu, B. Li, L. Chao, T. Niu, B. Du, H. Du, X. Ran, Y. Yang, Y. Xia, X. Gao, Y. Chen, W. Huang, *Nano Energy*, 2020, 73, 104803
49. C. Wu, W. Fang, Q. Cheng, J. Wan, R. Wen, Y. Wang, Y. Song, M. Li, *Angewandte Chemie International Edition*, 2022, 59, 21997
50. C. Shi, Q. Song, H. Wang, S. Ma, C. Wang, X. Zhang, J. Dou, T. Song, P. Chen, H. Zhou, Y. Chen, C. Zhu, Y. Bai, Q. Chen, *Advanced Functional Materials*, 2022, 32, 2201193
51. M. Badrooj, F. Jamali-Sheini, N. Torabi, *The Journal of Physical Chemistry C*, 2020, 124, 27136
52. G. Yuan, S. Qin, X. Wu, H. Ding, A. Lu, *Phase Transitions*, 2017, 91, 38
53. Q. Zhou, J. Duan, J. Du, Q. Guo, Q. Zhang, X. Yang, Y. Duan, Q. Tang, *Advanced Science*, 2021, 8, 2101418
54. A. Armigliato, R. Balboni, G. P. Carnevale, G. Pavia, D. Piccolo, S. Frabboni, A. Benedetti, A. G. Cullis, *Applied Physics Letters*, 2003, 82, 2172
55. K. Usuda, T. Numata, T. Irisawa, N. Hirashita, S. Takagi, *Materials Science and Engineering: B*, 2005, 124-125, 143
56. F. Uesugi, A. Hokazono, S. Takeno, *Ultramicroscopy*, 2011, 111, 995
57. M. Hytch, F. Houdellier, F. Hue, E. Snoeck, *Nature*, 2008, 453, 1086
58. M. U. Rothmann, W. Li, Y. Zhu, U. Bach, L. Spiccia, J. Etheridge, Y. B. Cheng, *Nature Communications*, 2017, 8, 14547
59. B. W. Jia, K. H. Tan, W. K. Loke, S. Wicaksono, S. F. Yoon, *Applied Surface Science*, 2017, 399, 220
60. J. Zhang, C. Huang, Y. Sun, H. Yu, *Advanced Functional Materials*, 2022, 2113367
61. R. Tovey, D. N. Johnstone, S. M. Collins, W. R. B. Lionheart, P. A. Midgley, M. Benning, C.-B. Schönlieb, *Inverse Problems*, 2021, 37, 015003
62. T. A. S. Doherty, S. Nagane, D. J. Kubicki, Y.-K. Jung, D. N. Johnstone, A. N. Iqbal, D. Guo, K. Frohna, M. Danaie, E. M. Tennyson, S. Macpherson, A. Abfalterer, M. Anaya, Y.-H. Chiang, P. Crout, F. S. Ruggeri, S. Collins, C. P. Grey, A. Walsh, P. A. Midgley, S. D. Stranks, *Science*, 2021, 374, 1598
63. B. Yang, D. Bogachuk, J. Suo, L. Wagner, H. Kim, J. Lim, A. Hinsch, G. Boschloo, M. K. Nazeeruddin, A. Hagfeldt, *Chemical Society Reviews*, 2022, 51, 7509
64. Y. Yalcinkaya, I. M. Hermes, T. Seewald, K. Amann-Winkel, L. Veith, L. Schmidt-Mende, S. A. L. Weber, *Advanced Energy Materials*, 2022, 12, 2202442
65. L. Kong, G. Liu, J. Gong, Q. Hu, R. D. Schaller, P. Dera, D. Zhang, Z. Liu, W. Yang, K. Zhu, Y. Tang, C. Wang, S. H. Wei, T. Xu, H. K. Mao, *Proceedings of the National Academy of Sciences of the United States of America*, 2016, 113, 8910
66. H. J. Queisser, E. E. Haller, *Science*, 1998, 281, 945
67. C. Deger, S. Tan, K. N. Houk, Y. Yang, I. Yavuz, *Nano Research*, 2022, 15, 5746
68. G. Kieslich, S. Sun, A. K. Cheetham, *Chemical Science*, 2015, 6, 3430
69. J. Wang, J. Yang, A. K. Opitz, D. Kalaev, A. Nenning, E. J. Crumlin, J. T. Sadowski, I. Waluyo, A. Hunt, H. L. Tuller, B. Yildiz, *Chemistry of Materials*, 2022, 34, 5138
70. L. A. Muscarella, B. Ehrler, *Joule*, 2022, 6, 2016
71. C. C. Boyd, R. Cheacharoen, T. Leijtens, M. D. McGehee, *Chemical Reviews*, 2019, 119, 3418
72. Z. Li, M. Yang, J.-S. Park, S.-H. Wei, J. J. Berry, K. Zhu, *Chemistry of Materials*, 2016, 28, 284
73. T. Chen, B. J. Foley, C. Park, C. M. Brown, L. W. Harriger, J. Lee, J. Ruff, M. Yoon, J. J. Choi, S.-H. Lee, *Science Advances*, 2016, 2, 1601650
74. Q. Han, S. H. Bae, P. Sun, Y. T. Hsieh, Y. M. Yang, Y. S. Rim, H. Zhao, Q. Chen, W. Shi, G. Li, Y. Yang, *Advanced Materials*, 2016, 28, 2253
75. S. Ma, S. H. Kim, B. Jeong, H. C. Kwon, S. C. Yun, G. Jang, H. Yang, C. Park, D. Lee, J. Moon, *Small*, 2019, 15, 1900219

DOI: 10.54227/elab.20230004

76. T. Wu, Y. Wang, Z. Dai, D. Cui, T. Wang, X. Meng, E. Bi, X. Yang, L. Han, *Advanced Materials*, 2019, 31, 1900605
77. W. Meng, K. Zhang, A. Osvet, J. Zhang, W. Gruber, K. Forberich, B. Meyer, W. Heiss, T. Unruh, N. Li, C. J. Brabec, *Joule*, 2022, 6, 458
78. K. Nishimura, D. Hirotani, M. A. Kamarudin, Q. Shen, T. Toyoda, S. Iikubo, T. Minemoto, K. Yoshino, S. Hayase, *ACS Applied Materials & Interfaces*, 2019, 11, 31105
79. H. Wang, C. Zhu, L. Liu, S. Ma, P. Liu, J. Wu, C. Shi, Q. Du, Y. Hao, S. Xiang, H. Chen, P. Chen, Y. Bai, H. Zhou, Y. Li, Q. Chen, *Advanced Materials*, 2019, 31, 1904408
80. J. Ma, M. Qin, Y. Li, T. Zhang, J. Xu, G. Fang, X. Lu, *Journal of Materials Chemistry A*, 2019, 7, 27640
81. H. Min, M. Kim, S.-U. Lee, H. Kim, G. Kim, K. Choi, J. H. Lee, S. I. Seok, *Science*, 2019, 366, 749
82. H. Cheng, C. Liu, J. Zhuang, J. Cao, T. Wang, W. Y. Wong, F. Yan, *Advanced Functional Materials*, 2022, 32, 2204880
83. Z. Zheng, F. Li, J. Gong, Y. Ma, J. Gu, X. Liu, S. Chen, M. Liu, *Advanced Materials*, 2022, 34, 2109879
84. H. Min, S.-G. Ji, S. I. Seok, *Joule*, 2022, 6, 2175
85. H. Zhang, Z. Chen, M. Qin, Z. Ren, K. Liu, J. Huang, D. Shen, Z. Wu, Y. Zhang, J. Hao, C. S. Lee, X. Lu, Z. Zheng, W. Yu, G. Li, *Advanced Materials*, 2021, 33, 2008487
86. X. Hu, C. Zhu, W. Zhang, H. Wang, J. Wang, F. Ren, R. Chen, S. Liu, X. Meng, J. Zhou, Y. Pan, X. Tian, D. Sun, S. Zhang, Y. Zhang, Z. Liu, Q. Chen, W. Chen, *Nano Energy*, 2022, 101, 107594
87. Y. Liu, A. V. Ievlev, L. Collins, A. Belianinov, J. K. Keum, M. Ahmadi, S. Jesse, S. T. Retterer, K. Xiao, J. Huang, B. G. Sumpter, S. V. Kalinin, B. Hu, O. S. Ovchinnikova, *Advanced Electronic Materials*, 2020, 6, 1901235
88. Y. Zhao, J. Duan, Y. Wang, X. Yang, Q. Tang, *Nano Energy*, 2020, 67, 104286
89. S. Y. Ju, W. I. Lee, H. S. Kim, *ACS Applied Materials & Interfaces*, 2022, 14, 39996
90. C. Zhang, S. Wu, L. Tao, G. M. Arumugam, C. Liu, Z. Wang, S. Zhu, Y. Yang, J. Lin, X. Liu, R. E. I. Schropp, Y. Mai, *Advanced Energy Materials*, 2020, 10, 2002004
91. J. Wu, Y. Cui, B. Yu, K. Liu, Y. Li, H. Li, J. Shi, H. Wu, Y. Luo, D. Li, Q. Meng, *Advanced Functional Materials*, 2019, 29, 1905336
92. Q. Zhou, J. Duan, X. Yang, Y. Duan, Q. Tang, *Angewandte Chemie International Edition*, 2020, 59, 21997
93. H. Bi, B. Liu, D. He, L. Bai, W. Wang, Z. Zang, J. Chen, *Chemical Engineering Journal*, 2021, 418, 129375
94. Y. Zhang, T. Kong, H. Xie, J. Song, Y. Li, Y. Ai, Y. Han, D. Bi, *ACS Energy Letters*, 2022, 7, 929
95. C. C. Zhang, S. Yuan, Y. H. Lou, Q. W. Liu, M. Li, H. Okada, Z. K. Wang, *Advanced Materials*, 2020, 32, 2001479
96. T. Liu, X. Zhao, X. Zhong, Q. C. Burlingame, A. Kahn, Y.-L. Loo, *ACS Energy Letters*, 2022, 7, 3531
97. W. Lv, Z. Hu, W. Qiu, D. Yan, M. Li, A. Mei, L. Xu, R. Chen, *Advanced Science*, 2022, 9, 2202028
98. K. Zheng, C. Liu, K. Yu, Y. Meng, X. Yin, S. Bu, B. Han, C. Liu, Z. Ge, *Chemical Engineering Journal*, 2022, 446, 137307
99. N. Yang, C. Zhu, Y. Chen, H. Zai, C. Wang, X. Wang, H. Wang, S. Ma, Z. Gao, X. Wang, J. Hong, Y. Bai, H. Zhou, B.-B. Cui, Q. Chen, *Energy & Environmental Science*, 2020, 13, 4344
100. J. Suo, B. Yang, J. Jeong, T. Zhang, S. Olthof, F. Gao, M. Grätzel, G. Boschloo, A. Hagfeldt, *Nano Energy*, 2022, 94, 106924
101. C. Wang, L. Ma, D. Guo, X. Zhao, Z. Zhou, D. Lin, F. Zhang, W. Zhao, J. Zhang, Z. Nie, *Journal of Materials Chemistry C*, 2020, 8, 3374
102. J. Luo, J. Xia, H. Yang, C. Sun, N. Li, H. A. Malik, H. Shu, Z. Wan, H. Zhang, C. J. Brabec, C. Jia, *Nano Energy*, 2020, 77, 105063

Biographies

Yuanyuan Zhao is an academic professor in the College of Mechanical and Electronic Engineering at Shandong University of Science and Technology (Qingdao, China). She received her Ph.D. from Ocean University of China. Her research interests cover all-inorganic perovskite solar cells, electrocatalytic hydrogen production.

Qunwei Tang is a senior Professor in the College of Chemical and Biological Engineering at Shandong University of Science and Technology. He is the dean of Institute of Carbon Neutrality and youth editor for eScience journal. His research interests cover perovskite solar cells and triboelectric nanogenerators. Up to date, he has published more than 350 papers in international journals such as Angewandte Chemie International Edition, Advanced Materials and two professional books. He has been listed in Chinese Most Cited Researchers, Career Scientific Impact (2021, 2022), World's Top 2% Scientists (2021, 2022). He also won the second prize of Guangdong Province Science and Technology Award (China), the first prize of Yunnan Province Science and Technology (China).